

The ensemble mean limit of the one-dimensional turbulence model and application to residual stress closure in finite volume large-eddy simulation

RANDALL J. McDERMOTT*^{†**}, ALAN R. KERSTEIN[‡], RODNEY C. SCHMIDT[§]
and PHILIP J. SMITH[†]

[†]The University of Utah, Salt Lake City, UT 84112, USA

[‡]Sandia National Laboratories, Livermore, CA 94551, USA

[§]Sandia National Laboratories, Albuquerque, NM 87185, USA

In order to gain insight into the one-dimensional turbulence (ODT) model of Kerstein [1] as it pertains to residual stress closure in large-eddy simulation (LES), we develop ensemble mean closure (EMC), an algebraic stress closure based on the mappings and time scale physics employed in ODT. To allow analytic determination of the stress the ODT model is simplified, conceptually, such that eddy events act upon a velocity field linearized by the local resolved scale strain. EMC can account for viscous effects, addressing the laminar flow finite eddy viscosity problem without implementation of the dynamic procedure [2]. The algebraic form of the model lends itself to analysis [3] and we are able to derive a theoretical value for the eddy rate constant. This value is a bound on the rate constant for full ODT subgrid closure and yields good results in LES of decaying isotropic turbulence with EMC.

1. Introduction

Large-eddy simulation (LES) is a powerful and increasingly important tool for modeling turbulent flow. However, the fidelity, cost and robustness of available subgrid closure models remain significant barriers to its greater application. Sagaut [4] provides an excellent survey of the wide range of models that have been proposed. Recently, a very different turbulence modeling approach, called ‘one-dimensional turbulence’ (ODT), has been developed by Kerstein *et al.* [1, 5] and applied to a range of problems amenable to analysis where turbulence-induced variations are geometrically simple. Although these two approaches are fundamentally different, it has been recognized (see, for example [6]) that ODT is a closure model candidate for LES. Schmidt *et al.* [7] used ODT to resolve the wall shear stress in a channel flow LES. Also, Schmidt *et al.* [8] and McDermott [9] have developed methods for using ODT as the LES bulk flow residual stress closure. Additionally, the ‘linear-eddy model’ (LEM) [10, 11], the predecessor of ODT, has matured and gained popularity for modeling turbulent reacting flows [12–14].

The ‘workhorse’ closure model for LES has been the Smagorinsky eddy viscosity model [15] and dynamic variations thereof [2, 16]. In this paper we introduce the ‘ensemble mean closure’ (EMC) model which establishes a link between ODT and the more conventional

*Corresponding author. Email: randy@crsim.utah.edu

**Current address: Cornell University, Ithaca, NY 14853, USA. Email: rjm75@cornell.edu

eddy viscosity methods. ODT closure for LES requires a length scale parameter (the maximum ODT eddy size), analogous to (but not the same as) the Smagorinsky filter width, and a rate constant, analogous to the Smagorinsky constant. As with the Smagorinsky model, for a given rate of residual energy production (i.e. the rate at which energy is transferred between resolved and unresolved scales) the rate constant and length scale are inversely proportional to one another and combine to form something like a turbulent mixing length.

Though Smagorinsky and ODT are both based on mixing length theory, ODT is a considerably more complex model that captures contributions from a spectrum of length scales. In fact, ODT is really more of a modeling *framework* than a unique model. The building blocks of this framework are: a one-dimensional mapping, an eddy time scale distribution and a one-dimensional Eulerian evolution equation. There exist a myriad of choices to fill each of these blocks. As such, and in no small part due to the stochastic sampling procedure, theoretical analysis of ODT is challenging. EMC was born of a desire to better understand ODT and to provide a theoretical basis for the empirically determined rate constant for coupled LES/ODT isotropic turbulence simulations. The resulting model has a validity of its own and, following ODT, accounts for viscous effects, addressing the laminar-flow finite eddy viscosity problem which plagues the constant coefficient Smagorinsky model.

2. EMC formulation

2.1 Overview

EMC is based on the mappings and time-scale physics employed in ODT. A simplified ODT model is envisioned in which eddy events act upon the LES-resolved velocity field and do not affect the likelihood of future events (reminiscent of the linear eddy model [10, 11]). For additional simplicity, in the region of an eddy the velocity field on the one-dimensional domain (here denoted by the coordinate r) is linearized to have a strain rate at location $r = y$ of $\mathcal{S}(y) = [\partial_r \bar{U}(r)]_{r=y}$ (see figure 1). The overbar here represents the conceptual spatial filtering (e.g. a sharp spectral cutoff at the grid Nyquist limit) of the instantaneous fully resolved

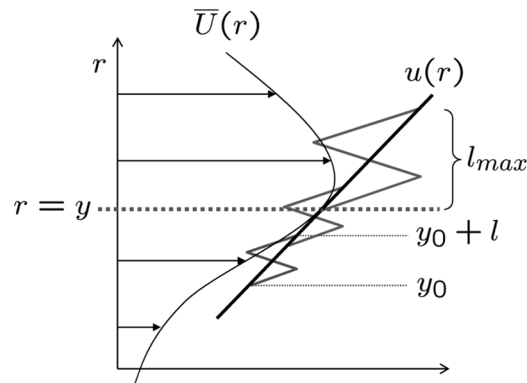


Figure 1. Ensemble mean closure is based on triplet maps applied to a velocity field that is linearized at a given location, y (i.e. $u(r) = \mathcal{S}(y)r + b$, where $\mathcal{S}(y) = [\partial_r \bar{U}(r)]_{r=y}$ and $\bar{U}(r)$ is the LES-scale filtered velocity field along the 1d domain). Only eddies within the interval $(y_0 < y < y_0 + l)$ affect the residual stress at y . In the sketch above the top eddy has barely any effect and the bottom eddy does not affect transport across y at all.

velocity field which results in the ‘LES-resolved’ velocity field, $\overline{U}(r)$. Eddy events act upon the linear field,

$$u(r) = \mathcal{S}(y)r + b, \quad (1)$$

where b is a constant that drops out in the derivations to follow. This linearity simplification allows for relatively simple analytical treatment of the mapping function (described in section 2.2). Finally, stresses are based on ensemble averaged momentum transport by ODT eddy events, rather than the usual stochastic eddy sampling. The resulting model is comparable to conventional LES closures such as the constant coefficient Smagorinsky model [15].

The form of the ensemble closure (which is independent of the linearization) is given, following Kerstein [17], by accounting for all eddy events which can affect a given location, y , on an ODT line. First, we find the amount of momentum displaced across y for an eddy parameterized by its starting location, y_0 , and length scale, l . The amount of momentum displaced, $\psi(y; y_0, l)$, is then multiplied by the event rate density of the eddy, given by $1/(l^2\tau)$, where τ is the eddy timescale (in general, $\tau = \tau(\overline{U}(r), l)$, but we will suppress the functional dependence until specific relationships are developed). With this, the form of the residual stress is

$$R(y) = \int_{l_{\min}}^{l_{\max}} \int_{y-l}^y \frac{\psi(y; y_0, l)}{l^2\tau} dy_0 dl. \quad (2)$$

The integration limits reflect the range of y_0 and l space which can possibly affect y . Completion of the model requires specification of ψ and τ .

As a point of clarification, we should mention that so far the model (2) is written to account for subgrid transport for one component along one direction only. The tensorial nature of the stress becomes evident when we consider multiple components and multiple directions. Being based on ODT, EMC is most naturally interpreted as a model for the unresolved advective stresses across control surfaces in a finite volume formulation. Application to three-dimensional finite volume closure is described in section 4. We will adopt the convention in this paper that, unless otherwise specified, $\tau_{ij}^R \equiv \overline{U_i U_j} - \overline{U_i} \overline{U_j}$ will denote the *definition* of the residual stress tensor (in the notation of Pope [18]) and R_{ij} will denote the *model* for τ_{ij}^R . In the EMC model the r coordinate becomes aligned with the x_j direction and the location, y , indicates the location of the flux surface for which we are computing the stress (i.e. the unresolved flux of component- i). Thus, $R_i(x_j = y)$, which we will write as simply $R_i(y)$, provides the macroscopic control volume analog of the microscopic R_{ij} stress tensor.

In what follows we will first establish the form of the momentum displacement function and timescale for the simplest version of ODT (one-component ODT [5], hereafter referred to as ‘vanilla ODT’). Then we will evaluate the integral (2). We will find close similarity between the resulting algebraic model and the Smagorinsky model [15] for the turbulent stress. We then consider the three-component vector formulation of ODT [1] (hereafter ‘vector ODT’). This version contains a ‘pressure scrambling’ model which redistributes energy among velocity components after a triplet map (see section 2.3). Next, we add complexity to the time scale, first by considering an energy-based time scale and then by considering the Reynolds number dependence. The one-dimensional analog of Lilly’s analysis [3] is then used to obtain a value for the rate constant. In section 4.5 we show results using EMC in LES of decaying isotropic turbulence. And, finally, we describe an extension of EMC to passive scalar subgrid transport in section 5.

2.2 EMC based on one-component ODT

It is useful to start with vanilla ODT because the salient features of this simple analysis extend to the more complex versions. In vanilla ODT momentum displacement is governed only by the triplet map (i.e. no pressure scrambling) and the time scale is based on the local strain rate. Similarly, in this section the EMC time scale, τ , is based on the resolved strain along the one-dimensional domain,

$$\frac{1}{\tau} = C_e |\mathcal{S}(y)|, \quad (3)$$

where C_e is the eddy rate constant and $|\mathcal{S}(y)|$ is the magnitude of the strain.

2.2.1 Triplet map momentum displacement. The triplet map (see figure 2) maps a field, $u(r)$, to $u(f(r))$, where

$$f(r) = y_0 + \begin{cases} 3(r - y_0) & \text{for } y_0 \leq r \leq y_0 + \frac{1}{3}l \\ 2l - 3(r - y_0) & \text{for } y_0 + \frac{1}{3}l \leq r \leq y_0 + \frac{2}{3}l \\ 3(r - y_0) - 2l & \text{for } y_0 + \frac{2}{3}l \leq r \leq y_0 + l \\ r - y_0 & \text{otherwise.} \end{cases} \quad (4)$$

The momentum driven across a point, y , by an eddy (y_0, l) in the positive direction is then given by

$$\psi(y; y_0, l) = \int_y^{y_0+l} [u(f(r)) - u(r)] dr. \quad (5)$$

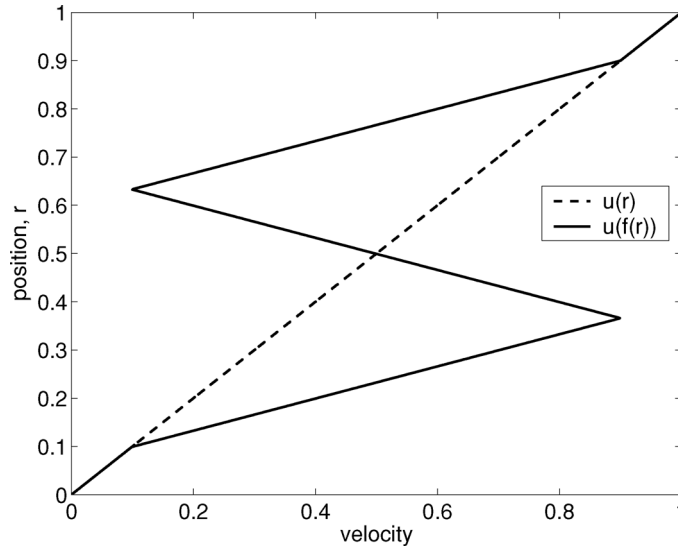


Figure 2. A triplet map of the linear field, $u(r)$, to $u(f(r))$, with $y_0 = 0.1$ and $l = 0.8$. Since position is given on the ordinate, this mapping represents a negative transport of momentum in the vertical direction.

Evaluating the integral (5) using equations (1) and (4) gives the following piecewise function for the momentum displacement,

$$\psi(y; y_0, l) = \begin{cases} -\mathcal{S}(y)(y_0 - y)^2 & \text{for } y_0 \leq y \leq y_0 + \frac{1}{3}l \\ \mathcal{S}(y)\left[2(y_0 - y)^2 + 2l(y_0 - y) + \frac{l^2}{3}\right] & \text{for } y_0 + \frac{1}{3}l \leq y \leq y_0 + \frac{2}{3}l \\ -\mathcal{S}(y)\left[(y_0 - y)^2 + 2l(y_0 - y) + l^2\right] & \text{for } y_0 + \frac{2}{3}l \leq y \leq y_0 + l \\ 0 & \text{otherwise.} \end{cases} \quad (6)$$

2.2.2 Integration. The integration limits in (2) discount eddies that do not transport momentum across the surface $r = y$. By making the variable transformation $-r = y_0 - y$ we can rewrite the integral (2) as

$$\begin{aligned} R(y) &= \int_{l_{\min}}^{l_{\max}} \int_{y_0+r-l}^{y_0+r} \frac{\psi(y; r, l)}{l^2 \tau(y)} dr dl, \\ &= \int_{l_{\min}}^{l_{\max}} \frac{1}{l^2 \tau(y)} \left[-\frac{1}{81} \mathcal{S}(y) l^3 - \frac{4}{81} \mathcal{S}(y) l^3 - \frac{1}{81} \mathcal{S}(y) l^3 \right] dl, \\ &= -\frac{2}{27} C_e |\mathcal{S}(y)| \mathcal{S}(y) \int_{l_{\min}}^{l_{\max}} l dl, \end{aligned} \quad (7)$$

where in the last step we have substituted (3) for the timescale. Integration over dl gives the final EMC result for the residual stress across the surface at location y for vanilla ODT,

$$R(y) = -\frac{1}{27} C_e (l_{\max}^2 - l_{\min}^2) |\mathcal{S}(y)| \mathcal{S}(y). \quad (8)$$

2.2.3 Comparison to Smagorinsky. In form, equation (8) closely resembles the Smagorinsky model [15] for the deviatoric part of the LES residual stress,

$$\tau_{ij}^R - \frac{1}{2} \delta_{ij} \tau_{kk}^R \approx -2(C_s \Delta)^2 |\bar{S}| \bar{S}_{ij}, \quad (9)$$

where, as mentioned, $\tau_{ij}^R \equiv \overline{U_i U_j} - \overline{U_i} \overline{U_j}$ is the exact residual stress, C_s is the Smagorinsky constant, Δ is the filter scale, $\bar{S}_{ij} \equiv \frac{1}{2}(\partial_j \overline{U_i} + \partial_i \overline{U_j})$, and $|\bar{S}| \equiv (2\bar{S}_{ij} \bar{S}_{ij})^{1/2}$ is the resolved strain magnitude. At this point in the EMC development the main difference between EMC and the Smagorinsky model is that the Smagorinsky model is a symmetric tensor. An inherent limitation of ODT, and hence EMC, is that no line-normal derivatives can be extracted. This makes any ODT derived closure non-symmetric. Hence it is important to cast ODT (and EMC) in terms of semi-discrete finite volume (FV) surface fluxes, which are symmetric only to leading order (see Appendix A for a detailed discussion).

Despite the difference in symmetry, an interesting comparison between EMC and Smagorinsky can be made at this point. Consider a flow in which the resolved motions resemble a simple shear in the r coordinate (and r is aligned with x_2 , for example). For high Reynolds number we have $l_{\max} \gg l_{\min}$ and (because the second term in \bar{S}_{ij} is zero) the EMC and Smagorinsky model parameters are related by

$$\frac{1}{27} C_e l_{\max}^2 = (C_s \Delta)^2. \quad (10)$$

If l_{\max} is set equal to the filter width and the rate constant, C_e , is set to unity, we find that $C_s^2 = 1/27$, or $C_s \approx 0.19$, in close agreement with the theoretical value of the Smagorinsky constant from Lilly's analysis [3] ($C_s \approx 0.17$ for a sharp spectral filter). In other words, if simplifying assumptions are applied to ODT which bring it more closely in line with the assumptions made by the Smagorinsky model (i.e. resolved strain is the driving force for energy dissipation), the geometry of the triplet map naturally produces a reasonable model constant.

2.3 EMC based on vector ODT

The vector formulation of ODT [1] carries all three velocity components, $u_i = [u, v, w]$, on a given line as a function of r . As an example, consider the ODT line aligned with the x_2 direction of an Eulerian reference frame in figure 3. For LES closure (section 4.1) we will similarly define ODT domains aligned with the x_1 and x_3 coordinates. The triplet map rearranges fluid elements which carry the scalar components u , v and w . The vector ODT model also accounts for 'return to isotropy' by conservatively redistributing the component energies after a mapping event. This redistribution procedure is henceforth referred to as the 'pressure-scrambling' model (see [1] for a detailed discussion). In this section we begin adding levels of complexity to EMC by accounting for the pressure scrambling model.

2.3.1 Kernel-based momentum displacement. In vector ODT the final velocity field involves addition of a kernel function, $c_i K(r)$, where the kernel is defined to be $K(r) = r - f(r)$ and c_i is a component specific amplitude, yet to be specified. Note that $\int_{-\infty}^{\infty} K(r) dr = 0$ and so the kernel does not change the momentum of an ODT domain (i.e. the kernel is not a momentum source or sink). The momentum driven across a specific point, y , however, is affected by the kernel:

$$\psi_i(y; y_0, l) = \int_y^{y_0+l} [u_i(f(r)) + c_i K(r) - u_i(r)] dr. \quad (11)$$

Due to the linear velocity profile and kernel definition, it can be shown that the momentum displacement function (with kernel based redistribution included) can be

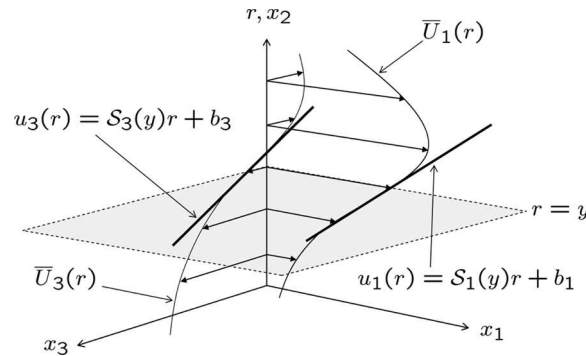


Figure 3. Conceptual velocity fields in the vector formulation, in this case with r aligned with the x_2 coordinate. The component 2 velocity fields, $\bar{U}_2(r)$ and $u_2(r)$, are defined analogously. The bold solid lines depict the linearizations that determine S_1 and S_3 at $r = y$.

expressed as

$$\psi_i(y; y_0, l) = \begin{cases} -(\mathcal{S}_i(y) - c_i(y))(y_0 - y)^2 & \text{for } y_0 \leq y \leq y_0 + \frac{1}{3}l \\ (\mathcal{S}_i(y) - c_i(y))\left[2(y_0 - y)^2 + 2l(y_0 - y) + \frac{l^2}{3}\right] & \text{for } y_0 + \frac{1}{3}l \leq y \leq y_0 + \frac{2}{3}l \\ -(\mathcal{S}_i(y) - c_i(y))\left[(y_0 - y)^2 + 2l(y_0 - y) + l^2\right] & \text{for } y_0 + \frac{2}{3}l \leq y \leq y_0 + l \\ 0 & \text{otherwise.} \end{cases} \quad (12)$$

2.3.2 Kernel amplitude. From [1] we find that the kernel amplitude can be written as (note that the index summation convention is implied throughout the paper unless otherwise specified)

$$c_i = \frac{27}{4l} \left(-v_{i,K} \pm \sqrt{v_{i,K}^2 + \alpha T_{ij} v_{j,K}^2} \right), \quad (13)$$

where

$$v_{i,K} \equiv \frac{4}{9l^2} \int_{y_0}^{y_0+l} u_i(r) [l + 2y_0 - 2r] dr, \quad (14)$$

$$T_{ij} \equiv \begin{bmatrix} -1 & \frac{1}{2} & \frac{1}{2} \\ \frac{1}{2} & -1 & \frac{1}{2} \\ \frac{1}{2} & \frac{1}{2} & -1 \end{bmatrix}, \quad (15)$$

and $0 \leq \alpha \leq 1$ is the fraction of the available energy (see section 2.4) which is to be redistributed among the components during an eddy event. The sign ambiguity in (13) is alleviated by requiring $c_i \rightarrow 0$ as $\alpha \rightarrow 0$, leading to the factor that multiplies the square root term in equation (18), below.

With the linearity assumption (1) equation (14) integrates to

$$v_{i,K} = -\frac{2}{27} \mathcal{S}_i(y) l. \quad (16)$$

The square root term in (13) is then written as

$$\sqrt{v_{i,K}^2 + \alpha T_{ij} v_{j,K}^2} = \sqrt{\beta_{ij} v_{j,K}^2} = -\frac{2}{27} l \sqrt{\beta_{ij} \mathcal{S}_j^2(y)}, \quad (17)$$

where $\beta_{ij} \equiv \delta_{ij} + \alpha T_{ij}$ and δ_{ij} is the Kronecker delta.

From these results the kernel amplitude, expressed in terms of the local strain rate, is

$$c_i(y) = \frac{1}{2} (\mathcal{S}_i(y) - \text{sgn}(\mathcal{S}_i(y)) \sqrt{\beta_{ij} \mathcal{S}_j^2(y)}). \quad (18)$$

Although nothing mathematically prohibits α from being considered a continuous free parameter in the range $[0, 1]$, it should be emphasized that only certain discrete choices lend themselves naturally to physical interpretation. These choices are $\alpha = 0, 2/3$ or 1 . When $\alpha = 0$ we recover vanilla ODT and when $\alpha = 1$ intercomponent available energy transfer is maximized [1]. Currently, standard practice in ODT is to set $\alpha = 2/3$, which equalizes intercomponent transfer of available energy (i.e. $\beta_{ij} = 1/3$). This choice is consistent with the return to isotropy mechanism that the ODT pressure scrambling model is intended to represent. Sensitivity to α has been considered previously [1, 19] and is considered here in section 4.5.

2.3.3 Integration. At this stage in the development of the model we wish to add only the complexity of energy redistribution. So, in this section we will retain the assumption that the eddy time scale varies inversely with strain rate. The difference between this and the model in section 2.2 is that here we need to account for all components in the strain rate definition. The time scale will, therefore, be given by

$$\frac{1}{\tau} = C_e |\mathcal{S}(y)|, \quad (19)$$

where

$$|\mathcal{S}(y)| \equiv \sqrt{\sum_j \mathcal{S}_j^2(y)}. \quad (20)$$

Using (18) we obtain the following relationship, which is needed in (12),

$$\mathcal{S}_i(y) - c_i(y) = \frac{1}{2} \mathcal{S}_i(y) + \frac{1}{2} \text{sgn}(\mathcal{S}_i(y)) \sqrt{\beta_{ij} \mathcal{S}_j^2(y)}. \quad (21)$$

The important thing to note is that the inclusion of $c_i(y)$ did not introduce any new dependencies on y_0 or l . Hence, the integration of (2) follows easily from section 2.2. The resulting EMC model, which includes pressure scrambling effects, is given by

$$R_i(y) = -\frac{1}{27} C_e (l_{\max}^2 - l_{\min}^2) |\mathcal{S}(y)| \left[\frac{1}{2} \mathcal{S}_i(y) + \frac{1}{2} \text{sgn}(\mathcal{S}_i(y)) \sqrt{\beta_{ij} \mathcal{S}_j^2(y)} \right]. \quad (22)$$

2.4 Energy-based time scale

In this section we examine an alternate definition of the eddy time scale which is used in the more recent ODT formulations [1, 20]. From the length and time scales we have available we can dimensionally construct an energy, E , as

$$E \sim \rho_0 l \frac{l^2}{\tau^2}, \quad (23)$$

where ρ_0 is a constant density (mass per unit length). We can then define the time scale as

$$\frac{1}{\tau} = C_e \sqrt{\frac{E}{\rho_0 l^3}}. \quad (24)$$

The modeling question becomes: what should we use for the energy? Kerstein and Wunsch [21] have suggested using the total available energy, defined by (26), below. This idea was originally introduced in the context of single-component ODT by Wunsch and Kerstein [20]. The definition of available energy is motivated as follows. The energy change for a given component, i , during an eddy event is given by

$$\Delta E_i = \frac{1}{2} \rho_0 \int_{y_0}^{y_0+l} [(u_i(f(r)) + c_i K(r))^2 - u_i(r)^2] dr. \quad (25)$$

Note that this formula generates a function, $\Delta E_i(c_i)$, which is quadratic in c_i . Also note that for $c_i = 0$ we have $\Delta E_i = 0$, since the triplet map is measure preserving. In figure 4 we plot the energy change function against the kernel amplitude for a linear field of slope \mathcal{S}_i . Another consequence of the linearity simplification is that if $c_i = \mathcal{S}_i$ there is no component i momentum transfer, as per (12), and hence no energy change. This is also confirmed in figure 4. The second zero crossing corresponds to $c_i = \mathcal{S}_i$.

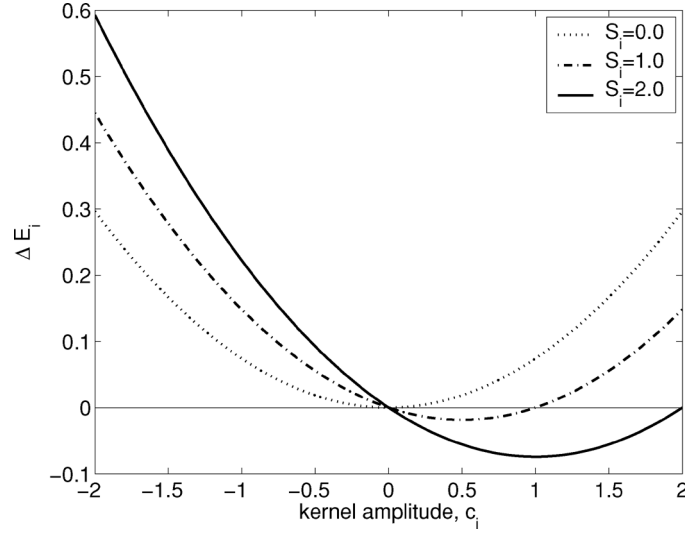


Figure 4. Component energy change (equation 25) as a function of kernel amplitude. Notice the zero crossings for different strain rates.

From the plot we can see that it is possible to *add* an infinite amount of energy to a given component. The amount of energy which can be *subtracted*, however, is bounded, and is equal to the minima of the curves in figure 4. It can be shown [1, 9] that this energy is given by

$$-\Delta E_i |_{\max} \equiv Q_i = \frac{27}{8} \rho_0 l v_{i,K}^2, \quad (26)$$

where $v_{i,K}$ is given by (14). With linearity (16) this reduces to

$$Q_i = \frac{1}{54} \rho_0 l^3 S_i^2(y). \quad (27)$$

Due to the restriction $\sum_i \Delta E_i = 0$, the amount of energy available for redistribution is bounded by, $\sum_i Q_i$. On the advice of Kerstein and Wunsch [21], we choose $E = \sum_i Q_i$ as the basis for the eddy time scale. From (24) we then have

$$\begin{aligned} \frac{1}{\tau} &= C_e \sqrt{\frac{\sum_i Q_i}{\rho_0 l^3}}, \\ &= \frac{C_e}{\sqrt{54}} |\mathcal{S}(y)|. \end{aligned} \quad (28)$$

Again, no new length scale dependencies have been introduced and so the EMC model is given by

$$R_i(y) = -\frac{1}{27} \frac{C_e}{\sqrt{54}} (l_{\max}^2 - l_{\min}^2) |\mathcal{S}(y)| \left[\frac{1}{2} \mathcal{S}_i(y) + \frac{1}{2} \operatorname{sgn}(\mathcal{S}_i(y)) \sqrt{\beta_{ij} \mathcal{S}_j^2(y)} \right]. \quad (29)$$

Note the subtle difference between (29) and (22). The factor of $1/\sqrt{54}$ shows up as a consequence of the choice for the time scale. This is the sort of insight we are seeking with regard to full ODT closure (see, for example [8]).

2.5 Reynolds number dependence

In real viscous flow an instability must be able to overcome the molecular forces of viscosity in order to propagate. Therefore, it does not make physical or computational sense to implement eddies which have lifetimes shorter than the viscous time scale. We impose this constraint on the model by requiring the available energy of an eddy to be larger than some threshold, else the eddy is rejected. This is done by making the following simple change to the energy scale [1],

$$E \sim \sum_j Q_j - E_v, \quad (30)$$

where E_v is a viscous energy scale given by

$$E_v = Z^2 \rho_0 \frac{v^2}{l}. \quad (31)$$

Here the constant of proportionality is taken to be Z^2 , because this allows Z to be interpreted as a critical Reynolds number for eddy turnover in ODT.

Inserting (30) into (24) and invoking the linearity assumption for the available energy (27), the formula for the time scale becomes

$$\frac{1}{\tau} = C_e \sqrt{\frac{1}{54} \sum_j \mathcal{S}_j^2(y) - Z^2 \frac{v^2}{l^4}}, \quad (32)$$

and τ now depends on l . Since the time scale does not depend on y_0 , the form of the stress closure can be written as (see Appendix B for details)

$$\begin{aligned} R_i(y) &= \int_{l_{\min}}^{l_{\max}} \frac{1}{\tau} \int_{y-l}^y \frac{\psi_i(y; y_0, l)}{l^2} dy_0 dl, \\ &= -\frac{1}{27} C_e \mathcal{F}(\mathcal{S}_i(y), l_{\max}, l_{\min}, Z, v) \left[\frac{1}{2} \mathcal{S}_i(y) + \frac{1}{2} \operatorname{sgn}(\mathcal{S}_i(y)) \sqrt{\beta_{ij} \mathcal{S}_j^2(y)} \right], \end{aligned} \quad (33)$$

where

$$\begin{aligned} \mathcal{F}(\mathcal{S}_i(y), l_{\max}, l_{\min}, Z, v) &= \sqrt{\frac{1}{54} \sum_j \mathcal{S}_j^2(y) l_{\max}^4 - (Zv)^2} - \sqrt{\frac{1}{54} \sum_j \mathcal{S}_j^2(y) l_{\min}^4 - (Zv)^2} \\ &\quad + Zv \left[\sin^{-1} \left(\frac{Zv}{\sqrt{\frac{1}{54} \sum_j \mathcal{S}_j^2(y) l_{\max}^4}} \right) \right. \\ &\quad \left. - \sin^{-1} \left(\frac{Zv}{\sqrt{\frac{1}{54} \sum_j \mathcal{S}_j^2(y) l_{\min}^4}} \right) \right]. \end{aligned} \quad (34)$$

Here notice that \mathcal{F} takes on the role previously played by $(l_{\max}^2 - l_{\min}^2) |\mathcal{S}(y)| / \sqrt{54}$ and should have identical behavior in the limit $v \rightarrow 0$. Indeed this is the case. For $v = 0$, equations (33) and (34) together reduce to (29). This limit is also confirmed by the asymptote in figure 5.

The following restrictions apply: Of course, $l_{\max} > l_{\min}$. But also, for a real solution we must have

$$\frac{1}{54} \sum_j \mathcal{S}_j^2(y) l_{\min}^4 - (Zv)^2 \geq 0. \quad (35)$$

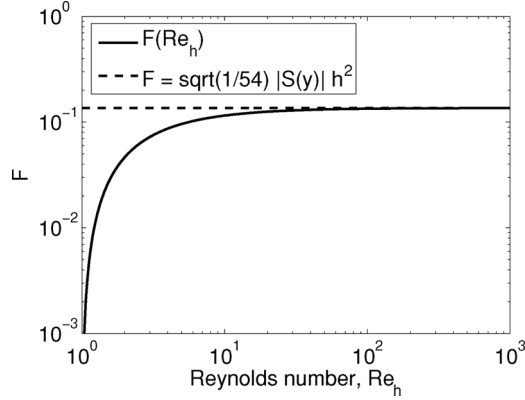


Figure 5. Reynolds number dependence of the EMC stress.

This rearranges to

$$\frac{Z\nu}{\sqrt{\frac{1}{54} \sum_j \mathcal{S}_j^2(y) l_{\min}^4}} \leq 1, \quad (36)$$

which is good, because this is the criterion for convergence of the infinite series for the arcsin function in (34).

Equation (34) can be simplified considerably by assuming that the parameter Z will be used to enforce the minimum eddy size. This amounts to assuming equality for (35). With this, the second term in \mathcal{F} vanishes and the argument of the last arcsin term becomes unity (note: $\sin^{-1}(1) = \pi/2$).

With $l_{\max} = h$ (where h is the LES grid spacing) the relevant local cell Reynolds number based on the grid-resolved strain rate is

$$\text{Re}_h \equiv \frac{|S| h^2}{\nu}. \quad (37)$$

Using this to rearrange (34) and assuming equality for (35) we obtain

$$\mathcal{F}(\text{Re}_h; Z, \nu) = \nu \left(\sqrt{\frac{1}{54} \text{Re}_h^2 - Z^2} + Z \left[\sin^{-1} \left(\frac{\sqrt{54}}{\text{Re}_h} Z \right) - \frac{\pi}{2} \right] \right). \quad (38)$$

To illustrate the functional form of (38), we require $\mathcal{F} \rightarrow 0$ as $\text{Re}_h \rightarrow 1$. This establishes the viscous cutoff as $Z = 1/\sqrt{54}$ and we have

$$\mathcal{F}(\text{Re}_h; \nu) = \nu \frac{1}{\sqrt{54}} \left(\sqrt{\text{Re}_h^2 - 1} + \sin^{-1} \left(\frac{1}{\text{Re}_h} \right) - \frac{\pi}{2} \right). \quad (39)$$

Equation (39) is plotted in figure 5. The Reynolds number is varied by adjusting the viscosity and maintaining a constant value of $\mathcal{S}_i(y)$. With this plot we are really examining the Reynolds number dependence of the stress itself because its Re_h dependence resides solely in the function \mathcal{F} . As expected, at high Re_h the stress is Reynolds number independent.

2.6 Comments on the maximum eddy size

It should be emphasized that C_e and l_{\max} are *not* independent model parameters. Choosing l_{\max} sets C_e and vice versa. Throughout the remainder of this paper we have adopted the

convention $l_{\max} = h$ for EMC because it is convenient for analysis. Though it is tempting to draw comparisons, l_{\max} is not a ‘filter width’ in the classical LES sense in that varying l_{\max} does not affect the definition of the local strain. As we will see in section 3, whatever one chooses for l_{\max} in EMC there is a rate constant, C_e , that will yield the correct rate of residual energy production (\mathcal{P}_r). The same is true for full ODT closure. With ODT, however, for a given \mathcal{P}_r the rate constant will be lower because ODT samples eddy events from an instantaneous timescale distribution, causing one eddy to cascade into several (more on this in section 3.2). Unlike EMC, with ODT we are also concerned with the quality of the subgrid statistics, which depend on \mathcal{P}_r and C_e . For a given \mathcal{P}_r , if C_e is set too high in ODT then energy will pile up in the high wavenumber subgrid ODT field (for a given molecular viscosity higher strains will be required to dissipate energy at the correct rate). The opposite is true if C_e is too low. Therefore, for ODT C_e should be determined by matching high wavenumber statistics for a given \mathcal{P}_r . The maximum eddy size must follow to match \mathcal{P}_r . There is evidence [8, 9] that the optimum maximum eddy-size for ODT subgrid closure is approximately $3h$.

3. Theoretical determination of the eddy rate constant

A limitation of stand-alone ODT is the need to empirically tune model parameters for different flows. In principle, merging ODT with LES should help alleviate this problem since LES can account for three dimensionality and complex boundary conditions. As previously mentioned, it is difficult to apply Lilly’s analysis [3] for determining the rate constant directly to ODT. Here, instead, we apply Lilly’s analysis to EMC, which, due to the recursive nature of ODT mappings, establishes an upper bound on the ODT rate constant. As shown in section 4.5, the theoretical constant works reasonably well for LES with ensemble mean closure.

3.1 Lilly’s analysis in one dimension

Lilly’s analysis assumes isotropy and equilibrium (i.e. that the production of residual kinetic energy equals the molecular dissipation rate) to determine a value for the model constant. First, we must establish a one-dimensional kinetic energy equation. We start with the filtered momentum equations in differential form,

$$\frac{\partial \bar{U}_i}{\partial t} + \frac{\partial (\bar{U}_i \bar{U}_j)}{\partial x_j} = -\frac{\partial \bar{P}}{\partial x_i} + \nu \frac{\partial^2 \bar{U}_i}{\partial x_j \partial x_j} - \frac{\partial \tau_{ij}^R}{\partial x_j}, \quad (40)$$

where the overbar represents a projection of the velocity field onto the finite dimensional LES space (e.g. a sharp spectral cutoff at the grid Nyquist limit). Multiplying this equation by \bar{U}_i , and defining $E_f \equiv \frac{1}{2} \bar{U}_i \bar{U}_i$, we have the transport equation for the filtered kinetic energy, left in terms of velocity gradients,

$$\frac{\partial E_f}{\partial t} + \frac{\partial (E_f \bar{U}_j)}{\partial x_j} + \frac{\partial}{\partial x_j} \left(\bar{U}_j \bar{P} - \nu \frac{\partial E_f}{\partial x_j} + \bar{U}_i \tau_{ij}^R \right) = -\tilde{\varepsilon}_f - \mathcal{P}_r, \quad (41)$$

where the filtered viscous pseudo-dissipation is here defined as

$$\tilde{\varepsilon}_f \equiv \nu \frac{\partial \bar{U}_i}{\partial x_j} \frac{\partial \bar{U}_i}{\partial x_j}, \quad (42)$$

and the production of residual kinetic energy is

$$\mathcal{P}_r \equiv -\tau_{ij}^R \frac{\partial \bar{U}_i}{\partial x_j}. \quad (43)$$

If (41) is averaged over a homogeneous region of space, such that the transport terms vanish, and if the flow is isotropic, we may write [9, 18] (no summation over y throughout this section)

$$\left\langle \frac{\partial E_f}{\partial t} \right\rangle = -3\nu \left\langle \frac{\partial \bar{U}_i}{\partial y} \frac{\partial \bar{U}_i}{\partial y} \right\rangle + 3 \left\langle \tau_{iy}^R \frac{\partial \bar{U}_i}{\partial y} \right\rangle. \quad (44)$$

We may now proceed with the analysis. The mean filtered pseudo-dissipation is given by (for a sharp spectral filter)

$$\langle \tilde{\varepsilon}_f \rangle = 3\nu \underbrace{\left\langle \frac{\partial \bar{U}_i}{\partial y} \frac{\partial \bar{U}_i}{\partial y} \right\rangle}_{\sum_i \mathcal{S}_i^2(y)} = 2\nu \int_0^{\pi/\Delta} \kappa^2 E(\kappa) d\kappa. \quad (45)$$

Inserting the Kolmogorov spectrum, $E(\kappa) = C_K \varepsilon^{2/3} \kappa^{-5/3}$ (see, for example, [18]), and integrating we get

$$3 \left\langle \sum_j \mathcal{S}_j^2(y) \right\rangle = 3 \langle |\mathcal{S}(y)|^2 \rangle = 2C_K \varepsilon^{2/3} \left[\frac{3}{4} \left(\frac{\pi}{\Delta} \right)^{4/3} \right], \quad (46)$$

or

$$\left(\frac{4}{3} \right)^{3/2} \left(\frac{3}{2C_K} \right)^{3/2} \left(\frac{\Delta}{\pi} \right)^2 \langle |\mathcal{S}(y)|^3 \rangle^* = \varepsilon, \quad (47)$$

where Δ is the filter width, ε is the molecular dissipation rate and C_K is Kolmogorov's universal constant. The asterisk on the average of the cube of the strain magnitude indicates that we have assumed the exponent and average commute. Using DNS, Meneveau and Lund [22] established the error in this assumption to be on the order of 20%.

Assuming equilibrium and substituting our model into the analysis (i.e. using $\tau_{iy}^R = R_i(y)$), we have

$$-3 \left\langle R_i(y) \frac{\partial \bar{U}_i}{\partial y} \right\rangle = \varepsilon. \quad (48)$$

Let us now plug in the EMC model from (29) with $\alpha = 0$. We start here because the physically preferred model value of $\alpha = 2/3$ requires an additional speculative assumption for this analysis which we will see below. Using (47) for ε , (48) becomes

$$-3 \left\langle \left[-\frac{1}{27} \frac{C_e}{\sqrt{54}} (l_{\max}^2 - l_{\min}^2) |\mathcal{S}(y)| \mathcal{S}_i(y) \right] \frac{\partial \bar{U}_i}{\partial y} \right\rangle = \left(\frac{4}{3} \right)^{3/2} \left(\frac{3}{2C_K} \right)^{3/2} \left(\frac{\Delta}{\pi} \right)^2 \langle |\mathcal{S}(y)|^3 \rangle, \quad (49)$$

We let $l_{\min} = 0$ and use the empirically determined value $C_K \approx 1.5$ (see, for example, [18]). Noting $\partial_y \bar{U}_i = \mathcal{S}_i(y)$ and $\mathcal{S}_i(y) \mathcal{S}_i(y) = |\mathcal{S}(y)|^2$, for $l_{\max} = \Delta$ the eddy rate constant is

$$C_e = 9 \left(\frac{4}{3.0} \right)^{3/2} \left(\frac{1}{\pi} \right)^2 \sqrt{54} \approx 1.4 \sqrt{54}. \quad (50)$$

Let us also analyze the case where $\alpha = 2/3$, equipartition of available energy in the pressure scrambling model. Using (29) for $R_i(y)$, taking $l_{\max} \gg l_{\min}$, and recalling $\beta_{ij} = 1/3$, we may

write (48) as

$$\frac{1}{9} \frac{C_e}{\sqrt{54}} l_{\max}^2 \left\langle |\mathcal{S}(y)| \left[\frac{1}{2} \underbrace{\mathcal{S}_i(y)\mathcal{S}_i(y)}_{|\mathcal{S}(y)|^2} + \frac{1}{2} \underbrace{\text{sgn}(\mathcal{S}_i(y))\mathcal{S}_i(y)}_{\|\mathcal{S}_i(y)\|_{L_1}} \frac{1}{\sqrt{3}} |\mathcal{S}(y)| \right] \right\rangle = \varepsilon. \quad (51)$$

The second term in the bracket contains the L_1 norm of the strain vector. Note that our current definition of the strain magnitude, $|\mathcal{S}(y)|$, is the L_2 norm of the strain vector. To proceed with the analysis we must make an assumption about how these norms are related. If all the strains are roughly equal in magnitude then we have the relation, $\|\mathcal{S}_i(y)\|_{L_1} \approx \sqrt{3} |\mathcal{S}(y)|$. When this is substituted into (51) the rate constant from (50) is unchanged. As we will see in later sections, however, results obtained using EMC in LES are slightly dependent on the choice of α , so this assumption seems rather poor. An alternative is to assume that two components of the strain are dominant (and equal), mimicking a local vortex [42]. This results in $\|\mathcal{S}_j(y)\|_{L_1} \approx \sqrt{2} |\mathcal{S}(y)|$. Using this in (51) gives

$$\underbrace{\left(\frac{1}{2} + \frac{1}{\sqrt{6}} \right)}_{\approx 0.91} \frac{1}{9} \frac{C_e}{\sqrt{54}} l_{\max}^2 \langle |\mathcal{S}(y)|^3 \rangle = \varepsilon. \quad (52)$$

The rate constant is, therefore, increased to

$$C_e \approx \frac{1.4}{0.91} \sqrt{54} \approx 1.5\sqrt{54}, \quad (53)$$

which is consistent with the trend in figure 6 (section 4.5).

3.2 Remarks on the rate constant for full ODT closure

Full ODT naturally exhibits cascade dynamics. Due to the cascade process and the particular mapping chosen (i.e. the triplet map) we expect the rate constant for full ODT closure to be less than that for EMC by roughly a factor of 3 (e.g. with $l_{\max} = h$, $C_e \approx \frac{1.4}{3} \sqrt{54}$). Preliminary results with ODT support this assertion [8, 9]. The specific factor, 3, results because once an eddy mapping takes place in ODT the local strain triples (due to the triplet map), making another eddy ($1/3$ the size or smaller) three times more likely to occur. Smaller eddies, however,

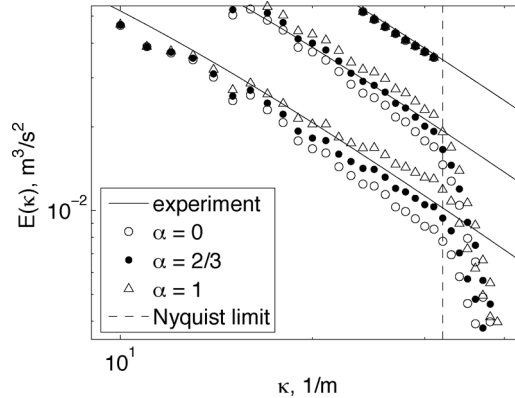


Figure 6. A zoom-in near the Nyquist limit of the three-dimensional energy spectra in decaying isotropic turbulence of the Kang *et al.* data with various choices of α and $C_e = 1.4\sqrt{54}$ and $Z = 0.14$. The solid lines represent the experimental data, respectively, from top to bottom, at $x/M = 20$ (initial condition), $x/M = 30$ and $x/M = 48$. The $x/M = 40$ data is omitted for clarity.

do not affect transport as much as larger eddies. The effective transport decreases geometrically as the length scale decreases. Therefore, accounting for the first recursive mapping event should be the leading order correction to the theoretical EMC rate constant when applied to ODT.

It is possible to confirm this assertion by performing Lilly's analysis with a stand-alone ODT model used to close the stress in (48), thus providing a theoretical link between C_e and l_{\max} for full ODT closure (we leave this for future work). To imagine how this would work first consider that it is not a requirement that the stress be determined algebraically. With EMC, for example, we could have stochastically implemented mapping events based on the linear field. For EMC the event distribution is uniform. Each time an eddy was sampled we would first compute and store the resulting stress and then re-linearize the field. The ensemble average of the stresses would yield the same result as the algebraic analysis. We can perform the same type of stochastic simulation with ODT, the simple difference being that we would not re-linearize the field and therefore account for stresses induced by the varying time scale distribution (i.e. recursive mappings).

Regarding the cascade, it should be appreciated that the geometric increase in frequencies and the properties of the triplet map are what allow ODT to produce a $-5/3$ energy spectrum [5]. No such physical mechanism is present in EMC. Like other eddy viscosity closures, the EMC model only indirectly represents the energy cascade through the assumption of equilibrium (i.e. production equals dissipation).

4. Ensemble mean closure in finite volume LES

In this section we apply the EMC model, so far derived for multiple components in a single direction, to subgrid closure in a three-dimensional finite volume LES. We first describe the LES formulation and numerical methods employed. We then present results for decaying isotropic turbulence, examining sensitivity to the pressure scrambling model and establishing an empirical value for the viscous cutoff. We then compare statistical measures of the resolved field with high Re wind tunnel data [23] including structure function probability density, hyper-flatness factors, residual energy production and the probability density function (PDF) of the residual stress.

4.1 Finite volume governing equations

The formulation presented here is similar to Schumann [24] and is chosen to make use of a combination of the *finite volume* (FV) and *semi-discrete* approaches for the numerical solution of scalar conservation laws. Both methods receive considerable attention in Lomax *et al.* [25] and Verstappen and Veldman [26]. The integral form of the governing equations for mass and momentum conservation of an incompressible fluid are, respectively,

$$\oint_S U_j n_j dS = 0 \quad (54)$$

and

$$\frac{d}{dt} \int_V U_i dV = - \int_S (U_i U_j + P \delta_{ij} + \tau_{ij}) n_j dS, \quad (55)$$

where P is the hydrodynamic pressure, $\tau_{ij} = -\nu(\partial_j U_i + \partial_i U_j)$ is the viscous stress and ν is the kinematic viscosity. A principal advantage of the FV method is that discrete conservation of solution variables is obtained *a priori*. Care must be taken, however, to ensure discrete conservation of kinetic energy (see, for example, [26–28]). Though the method is suited for irregular and unstructured grids, here we consider only simple cubic control volumes (CVs) of

side h . Thus, the CV volume is $V = h^3$ and the surface area of a given CV face k is $S_k = h^2$. We define a surface filtered field, $\bar{\phi}^{(j)}(\mathbf{x})$, to be the average value of the scalar, $\phi(\mathbf{x})$, on a two-dimensional planar surface normal to the x_j direction. That is, we apply two orthogonal tophat filters to the scalar field. For example, the x_1 surface-filtered field for a three-dimensional domain is

$$\bar{\phi}^{(1)}(\mathbf{x}) \equiv \frac{1}{h^2} \int_{x_3-h/2}^{x_3+h/2} \int_{x_2-h/2}^{x_2+h/2} \phi(\mathbf{x}') dx'_2 dx'_3. \quad (56)$$

The ‘volume-filtered’ or ‘cell-average’ field is then given by applying a one-dimensional tophat filter to the surface-filtered field (in the direction normal to the surface):

$$\begin{aligned} \tilde{\phi}(\mathbf{x}) &\equiv \frac{1}{h^3} \int_{x_3-h/2}^{x_3+h/2} \int_{x_2-h/2}^{x_2+h/2} \int_{x_1-h/2}^{x_1+h/2} \phi(\mathbf{x}') dx'_1 dx'_2 dx'_3 \\ &= \frac{1}{h^3} \int_{V(\mathbf{x})} \phi dV = \frac{1}{h} \int_{x_j-h/2}^{x_j+h/2} \bar{\phi}^{(j)}(\mathbf{x}') dx'_j \perp S_j. \end{aligned} \quad (57)$$

The net result is what Pope [18] refers to as an ‘anisotropic box filter’ and is reference frame dependent, an inherent characteristic of the finite volume approach which is tolerated because of the practical advantages of the method.

To obtain the finite volume discretization we sample the filtered fields from a discrete space. For example, $\tilde{\phi}(\mathbf{x}) \rightarrow \tilde{\phi}(i, j, k)$. By inserting (56) and (57) into (55) we end up with the FV momentum equation:

$$\frac{d\tilde{U}_i}{dt} = -\frac{S_k}{V} n_{kj} (\overline{U_i U_j})^{(k)} + \bar{P}^{(k)} \delta_{ij} + \bar{\tau}_{ij}^{(k)}, \quad (58)$$

where n_{kj} is a matrix of unit normal vectors for each face k . The summation convention applies (except for superscripts, which are used here simply to reference a particular surface) and hence $\frac{S_k}{V} n_{kj} = \frac{h^2}{h^3} n_{kj} = \frac{1}{h} n_{kj}$ is the finite volume ‘divergence’ operator. For a cubic CV aligned with a cartesian reference frame this matrix is simply

$$n_{kj} = \begin{bmatrix} 1 & 0 & 0 \\ -1 & 0 & 0 \\ 0 & 1 & 0 \\ 0 & -1 & 0 \\ 0 & 0 & 1 \\ 0 & 0 & -1 \end{bmatrix}. \quad (59)$$

In this notation the number of rows in n_{kj} equals the number of faces of the CV and the number of columns equals the dimension of the domain (e.g. 3 columns for a three-dimensional problem). Each row stores the unit normal vector for that face. S_k is a row vector (i.e. a 1×6 matrix) of CV face areas, all equal to h^2 in this case. This notation is also convenient for unstructured grids with irregular CV shapes.

4.2 FV LES formulation

Equation (58) is obviously just a redefinition of terms in the integral momentum equation but highlights the fact that the FV approach employs two different filters. The challenge of a numerical method is to approximate the surface integrals based on cell-average (volume-filtered) data. In LES we have the additional difficulty that the underlying continuous data

are not guaranteed to be smooth in any sense. In this paper we introduce a decomposition of the advective stress into ‘numerical’ and ‘residual’ components. The residual stress is thus defined by the difference between the exact surface-filtered flux (e.g. the surface filter (56) applied to a DNS-like field) and the numerical approximation used for the advective flux. We are left with the following FV LES equations:

$$\frac{d\tilde{U}_i}{dt} = -\frac{S_k}{V} n_{kj} \left(\overline{U}_i^{x_j} \overline{U}_j^{x_i} + \overline{P}^{(k)} \delta_{ij} + \overline{\tau}_{ij}^{(k)} + \tau_{ij}^{R,(k)} \right), \quad (60)$$

where

$$\tau_{ij}^{R,(k)} \equiv \overline{U}_i U_j^{(k)} - \overline{U}_i^{x_j} \overline{U}_j^{x_i}. \quad (61)$$

Note the distinction between the numerical advective flux defined by, for example, an interpolant (note that it is also common to invoke an ENO reconstruction [29, 30]), here denoted by an overbar with superscript x_i , and the flux defined by application of a surface filter to the DNS-like velocity field, here denoted by an overbar with superscript (k) . The first term in (61), the surface-filtered term, is the application of (56) to the dyadic $U_i U_j$ on surface k . The second term depends on the numerical method and for our calculations is given by (66) in section 4.4 where we have followed the notation of Morinishi *et al.* [28]. The point to be made is that even though (60) already contains reference to the numerical procedure to be employed it is still an exact representation of the CV momentum balance.

4.3 Physical interpretation of residual stress closure

Following [31] the residual stress (61) can be decomposed into a Leonard stress (\mathcal{L}_{ij}), cross stresses (\mathcal{C}_{ij}), and a Reynolds stress (\mathcal{R}_{ij}):

$$\tau_{ij}^{R,(k)} = \underbrace{\overline{U}_i^{x_j} \overline{U}_j^{x_i}^{(k)} - \overline{U}_i^{x_j} \overline{U}_j^{x_i}}_{\mathcal{L}_{ij}} + \underbrace{\overline{U}_i^{x_j} \overline{U}_j^{(k)} + \overline{U}_i \overline{U}_j^{x_i}^{(k)}}_{\mathcal{C}_{ij}} + \underbrace{\overline{U}_i' \overline{U}_j'^{(k)}}_{\mathcal{R}_{ij}}, \quad (62)$$

where $U_j' \equiv U_j - \overline{U}_j^{x_i}$. The numerical advective term is constant on a face and so in this formulation the Leonard term is identically zero. The cross stresses survive, however, because the velocity fluctuation is defined by the interpolant, not the surface filter. Notice that if we had defined the fluctuation as $U_j' \equiv U_j - \overline{U}_j^{(k)}$ we would have a Reynolds decomposition and the cross terms would vanish as in Schumann’s formulation [24]. We have chosen the former decomposition because of its consistency with the physical picture of ODT.

In principle, a triplet map represents subgrid advection along the ODT line direction. That is, an ‘eddy event’ is a model for U_j' (taking the convention consistent with the divergence operator that component i is being advected in the j direction). Since full ODT carries the scalars U_i on a given line then the mapping events physically represent a model for the Reynolds stress and the first term of the cross stress. (A discussion on capturing the effects of the second cross stress in the full ODT approach is beyond the scope of this paper. The interested reader is referred to McDermott [9] and Schmidt *et al.* [8]. The physical picture in EMC is somewhat different. Here eddy events map only the $\overline{U}_i^{x_j}$ field. Therefore, EMC is really best thought of as a model for the first term of the cross stress, which, like EMC, is not symmetric (recall the discussion in section 2.2.3). In the present case, however, we assume EMC to account for all of the residual energy production, understanding that it should be possible to combine EMC with other models to produce a better physical picture of the subgrid transport, in the spirit of the ‘mixed model’ of Bardina *et al.* [32], for example).

4.4 Numerical method

In the semi-discrete approach one first approximates the surface-filtered fluxes using the cell averages at a given time, t . One is then left with the task of solving a coupled set of ordinary differential equations in time. Our code uses a uniform mesh with the staggered grid storage arrangement of Harlow and Welch [33] (equivalently see Morinishi *et al.* [28]) and the third-order Runge-Kutta (RK3) time integration scheme of Shu and Osher [34]. Following Suresh and Huynh [35], we first describe the time advancement for a single forward Euler step and then extend this to the RK3 scheme.

After Chorin [36], continuity (54) is integrated with (60) as follows: Let W_i^n represent the discrete LES state at time, t^n . We desire an explicit update of the following form,

$$W_i^{n+1} = W_i^n + \Delta t \left[F(W_i^n) - \frac{\delta\varphi}{\delta x_i} \right], \quad (63)$$

where $\Delta t = t^{n+1} - t^n$, W_i^{n+1} is divergence free (discretely), $F(\cdot)$ is the explicit advection-diffusion-subgrid operator (yet to be defined) and φ is the scalar used to enforce the continuity constraint. (We have made these changes in notation from the LES formulation in the previous section in order to avoid the confusion often related to explicit filtering. The LES state is never truly defined by an explicit filtering step. One never filters a DNS field, U , to obtain \bar{U} , for example. Rather, the LES state is defined by the numerical procedure.) In the notation of Morinishi *et al.* [28] the second-order difference (in the x_1 direction, for example) is defined by

$$\left. \frac{\delta\phi}{\delta x_1} \right|_{x_1, x_2, x_3} \equiv \frac{\phi(x_1 + h/2, x_2, x_3) - \phi(x_1 - h/2, x_2, x_3)}{h}. \quad (64)$$

The spatial discretization operator, $F(W_i)$, is decomposed as

$$F(W_i) = -\frac{\delta}{\delta x_j} \left[\bar{W}_i^{x_j} \bar{W}_j^{x_i} + v \left(\frac{\delta W_i}{\delta x_j} + \frac{\delta W_j}{\delta x_i} \right) + R_{ij} \right], \quad (65)$$

where the terms on the right-hand side of (65) are, respectively, the advective, diffusive and subgrid forces. For the advective operator we employ the kinetic energy preserving second-order staggered grid scheme of Harlow and Welch [33]. Here we employ Morinishi's notation [28] for the Harlow and Welch scheme. The interpolation operator used in (65) is defined as follows. The second-order interpolation (in the x_1 direction, for example) is

$$\bar{\phi}^{x_1} |_{x_1, x_2, x_3} \equiv \frac{\phi(x_1 + h/2, x_2, x_3) + \phi(x_1 - h/2, x_2, x_3)}{2}. \quad (66)$$

We take R_{ij} to represent a model for the residual stress (61). One can envision several options for implementation of the EMC model on staggered grids. The reader is referred to Appendix C for details of the specific method employed here.

Since the correct 'pressure' field, $\varphi(\mathbf{x})$, needed to make the LES state divergence free is unknown, we first compute a velocity field update based on a guess for the pressure field. Setting the guess for the pressure field to zero gives the predictor step,

$$W_i^* = W_i^n + \Delta t [F(W_i^n)]. \quad (67)$$

Subtracting (67) from (63) yields the so called pressure projection,

$$W_i^{n+1} = W_i^* - \Delta t \frac{\delta\varphi}{\delta x_i}. \quad (68)$$

Taking the discrete divergence of (68) and setting $\delta_i W_i^{n+1} = 0$ results in the Poisson equation for the pressure,

$$\frac{\delta}{\delta x_i} \frac{\delta \varphi}{\delta x_i} = \frac{1}{\Delta t} \frac{\delta W_i^*}{\delta x_i}, \quad (69)$$

which is solved for φ , and the result used in (68). From here on we refer to combined steps (69) and (68), in that order, as the projection operator, $\mathcal{P}(\cdot)$. For example, $W_i^{n+1} = \mathcal{P}(W_i^*)$, is the projection of W_i^* , from (67), onto a divergence free space.

With the projection established, the RK3 scheme can be written as follows. Let $W_i^{(0)} = W_i^n$. Then, proceeding from left to right, top to bottom:

$$\begin{aligned} W_i^{*(1)} &= W_i^{(0)} + \Delta t F(W_i^{(0)}), & W_i^{(1)} &= \mathcal{P}(W_i^{*(1)}), \\ W_i^{*(2)} &= \frac{3}{4} W_i^{(0)} + \frac{1}{4} \Delta t F(W_i^{(1)}), & W_i^{(2)} &= \mathcal{P}(W_i^{*(2)}), \\ W_i^{*(3)} &= \frac{1}{3} W_i^{(0)} + \frac{2}{3} \Delta t F(W_i^{(2)}), & W_i^{(3)} &= \mathcal{P}(W_i^{*(3)}), \end{aligned} \quad (70)$$

and $W_i^{n+1} = W_i^{(3)}$. As a practical note, it is important that the sequence of averaging and projection be kept as they are in (70) to avoid accumulation of numerical mass divergence in the system.

4.5 Results for decaying isotropic turbulence

We start the EMC validation by comparing results to the active grid high Re wind-tunnel data of Kang *et al.* [23]. We use a uniform mesh spacing, $h = L/N$, where, following Kang *et al.* [23], $L = 5.12$ m and $N = 64$. Hence, $h = 0.08$ m, corresponding to the filter scale Δ_4 in the Kang data. All simulations were run with an advection limiting CFL of $\frac{\Delta t \|\mathbf{W}\|_\infty}{h} = 0.25$, which is quite conservative for the RK3 time integration scheme. The non-dimensional times for the data points are: $x/M = 20$ (initial condition), 30, 40 and 48 (note that x is the distance downstream of the active grid and M is the distance between rotation shafts of the active grid; see [23] for more details). These correspond to dimensional times of: $t = 0, 0.15, 0.30$ and 0.42 s in our simulations.

The initial condition for the velocity field was generated by the following procedure. Fourier modes with random phases were superimposed to match the initial spectrum of the data. This field was then allowed to evolve for a short period (2–3 time steps) during which time the energy would decay and coherent turbulent structure would develop. Energy was then injected back into the Fourier modes such that the spectrum of the initial condition again matched the spectrum of the initial data. This process was repeated several times until the coherent structures stabilized. The initial field was then filtered with a spectral cutoff at the grid Nyquist limit (π/h).

We first tested the sensitivity of EMC to the choice of pressure scrambling model. We used the theoretically determined rate constant $C_e = 1.4\sqrt{54}$ (based on $l_{\max} = h$) and viscous cutoff $Z = 1/\sqrt{54} \approx 0.14$. In section 3 it is shown that the uncertainty associated with the commutativity assumption in (47) is greater than the α sensitivity of the theoretical rate constant. Additionally, it is shown that increasing α decreases the decay rate. This was demonstrated in figure 6. Due to assumptions in Lilly's analysis (e.g. commutation of the averaging operation and the shape of the filter) the theoretical rate constant for a given α leads to imperfect results in practice (notice that the $\alpha = 0$ case is too dissipative). Figure 7, however, demonstrates that Lilly's analysis works well for quantifying the effects of α on the decay rate. Here the theoretically linked values for C_e and α are used and very similar results are achieved. This lends support to the assumption that two components of the strain dominate locally (see section 3).

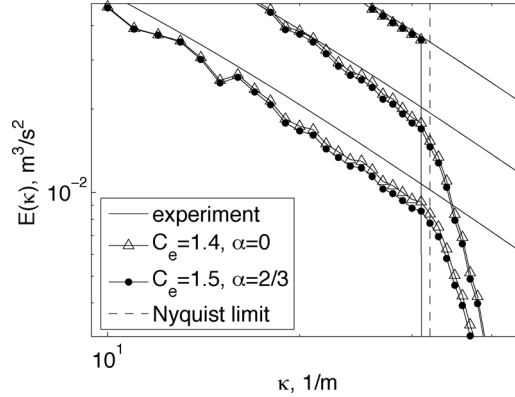


Figure 7. A zoom-in near the Nyquist limit of the three-dimensional energy spectra for the Kang *et al.* data. Based on Lilly's analysis (section 3) with the assumption that two components of the strain vector are dominant and equal, the two C_e/α combinations shown here should yield the same results. Note that the rate constant in the legend has been normalized by $\sqrt{54}$. The solid lines represent the experimental data, respectively, from top to bottom, at $x/M = 20$ (initial condition), $x/M = 30$ and $x/M = 48$. The $x/M = 40$ data is omitted for clarity.

Based on figure 6 the standard ODT value of $\alpha = 2/3$ (i.e. equipartition of energy in the pressure scrambling model) seems to yield the best results when used with $C_e = 1.4\sqrt{54}$ (see also figure 8). We will see further evidence supporting the choice $\alpha = 2/3$ in section 5.

With these baseline parameters established (i.e. $C_e = 1.4\sqrt{54}$ and $\alpha = 2/3$), we next tested the model against the low Re data of Comte-Bellot and Corrsin (CBC) [37]. Viscous effects are important in this data set for a well-resolved LES, testing the model's Re dependence. Following de Bruyn Kops [38], we used a periodic box of side $L = 9 \times 2\pi$ centimeters (≈ 0.566 m) and $\nu = 1.5 \times 10^{-5}$ m²/s for the kinematic viscosity. The non-dimensional times for this data set are $x/M = 42$ (initial condition), 98 and 171. These correspond to dimensional times of $t = 0.00$, 0.28 and 0.66 s in our simulations. In figure 9 the LES three-dimensional energy spectra are compared to the CBC data for two values of the viscous cutoff. The initial guess of $Z = 1/\sqrt{54} \approx 0.14$ allows the model to dissipate energy too quickly, indicating the model is not turning itself off in laminar flow regions. The viscous cutoff was tuned to $Z = 3.0$

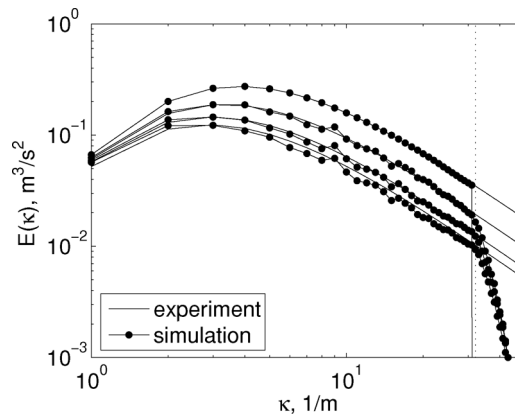


Figure 8. Three-dimensional energy spectra for the Kang data with $C_e = 1.4\sqrt{54}$, $\alpha = 2/3$ and $Z = 0.14$. The solid lines represent the experimental data, respectively, from top to bottom, at $x/M = 20$ (initial condition), $x/M = 30$, $x/M = 40$ and $x/M = 48$.

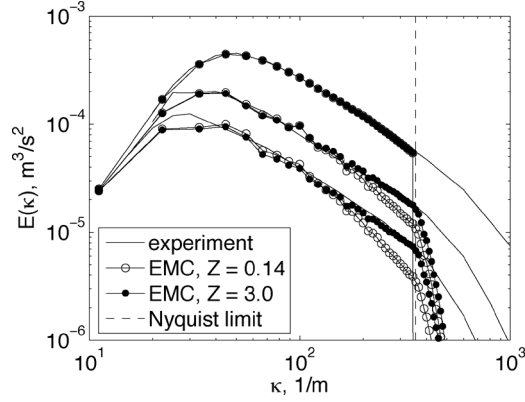


Figure 9. Three-dimensional energy spectra for the CBC data comparing values of the viscous cutoff, Z (note: $1/\sqrt{54} \approx 0.14$) with $C_e = 1.4\sqrt{54}$ and $\alpha = 2/3$. The solid lines represent the experimental data, from top to bottom, at $x/M = 42$ (initial condition), $x/M = 98$ and $x/M = 171$.

to match the CBC data. In figure 10 we have rerun the Kang *et al.* data with the new value for the viscous cutoff. As should be the case, at high Reynolds number the viscous cutoff does not affect the results and the spectra for the two different cutoff values are identical.

To gain further insight into the characteristics of the resolved field we make some further comparisons with the Kang *et al.* data (<http://pegasus.me.jhu.edu/~meneveau/datasets/actgriddata.html>). We first check the structure function PDF at two different length scales. The longitudinal structure function of the filtered velocity field is given by

$$\delta\tilde{U}_1(x_1, x_2, x_3) = \tilde{U}_1(x_1 + r, x_2, x_3) - \tilde{U}_1(x_1, x_2, x_3), \quad (71)$$

where r is the separation distance. Here the tilde over the velocity indicates that the structure function is computed using the cell average velocities (i.e. the LES state, equivalent to W in section 4.4). The transverse structure function is given by

$$\delta\tilde{U}_2(x_1, x_2, x_3) = \tilde{U}_2(x_1 + r, x_2, x_3) - \tilde{U}_2(x_1, x_2, x_3). \quad (72)$$

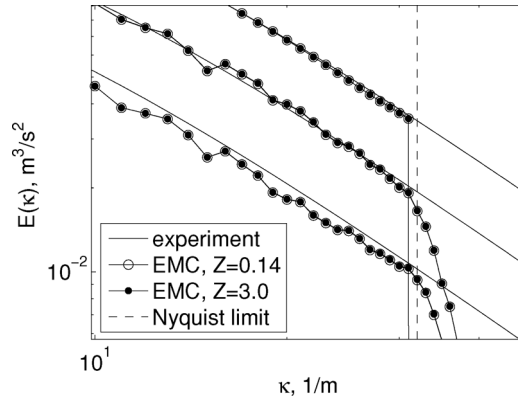


Figure 10. Three-dimensional energy spectra of the Kang *et al.* data. EMC simulations ($C_e = 1.4\sqrt{54}$ and $\alpha = 2/3$) with different values of Z are shown near the Nyquist limit demonstrating that the viscous cutoff is not significant for this high-Re flow at 64^3 resolution. The solid lines represent the Kang experimental data, respectively, from top to bottom, at $x/M = 20$ (initial condition), $x/M = 30$ and $x/M = 48$. The $x/M = 40$ data has been omitted for clarity.

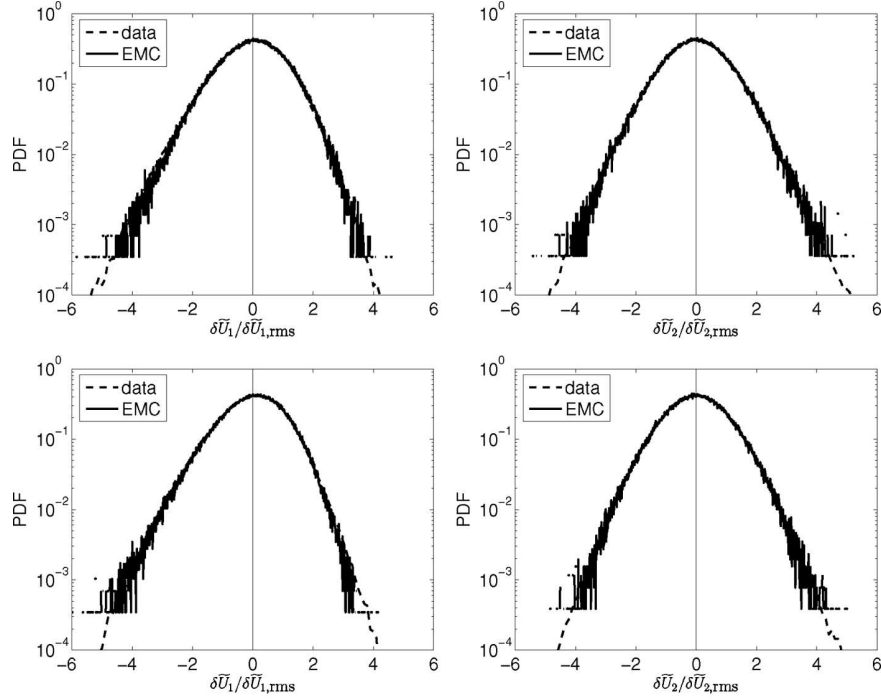


Figure 11. Longitudinal ($\delta\tilde{U}_1$) and transverse ($\delta\tilde{U}_2$) structure function PDF normalized by the rms for data at station $x/M = 48$. The top plots are for a separation distance of $r = h$ (see equations (71) and (72)) and the bottom plots are for a separation distance of $r = 2h$.

The PDFs of these quantities normalized by the root mean square (rms) value are plotted (for the data at station $x/M = 48$, the last data point) in figure 11 for two values of separation distance corresponding to $r = h$ and $r = 2h$. Here $h = \Delta_4 = 0.08$ m is the grid spacing in the simulation (Δ_4 is the notation used in Kang *et al.* [23] for this filter width). No explicit filtering was performed, and hence we recognize that there is ambiguity in the ‘implied filter’ kernel. This is part of the motivation for the following comparisons. In this case the LES using EMC does a good job of matching the data, exhibiting the skewness of the longitudinal structure function pdf and the symmetry of the transverse structure function pdf at both resolutions. Intermittency (the ability to capture the breadth of the distribution) is predicted well to a certain point, although the distribution is ‘fuzzy’ due to the relatively low resolution of the simulation and the shape of the implied filter which differs considerably from Gaussian (i.e. it is closer to a spectral truncation).

Deviations from Gaussian behavior are examined, following Kang *et al.* [23], by comparing the simulation results with measured hyper-flatness factors. The hyper-flatness of order n (where $n \geq 2$ is an even integer) is defined by (no summation over i)

$$F_{\delta\tilde{U}_i}(n) \equiv \frac{\langle (\delta\tilde{U}_i)^n \rangle}{(\delta\tilde{U}_{i,rms})^n}. \quad (73)$$

Note that $F(2) = 1$. For a Gaussian random variable with unit variance the hyper-flatness is given by

$$F_G(n) = \frac{2^{(n+1)/2}}{\sqrt{2\pi}} \Gamma\left(\frac{n+1}{2}\right), \quad (74)$$

where $\Gamma(\cdot)$ is the Gamma function, $\Gamma(z) = \int_0^\infty t^{z-1} e^{-t} dt$.

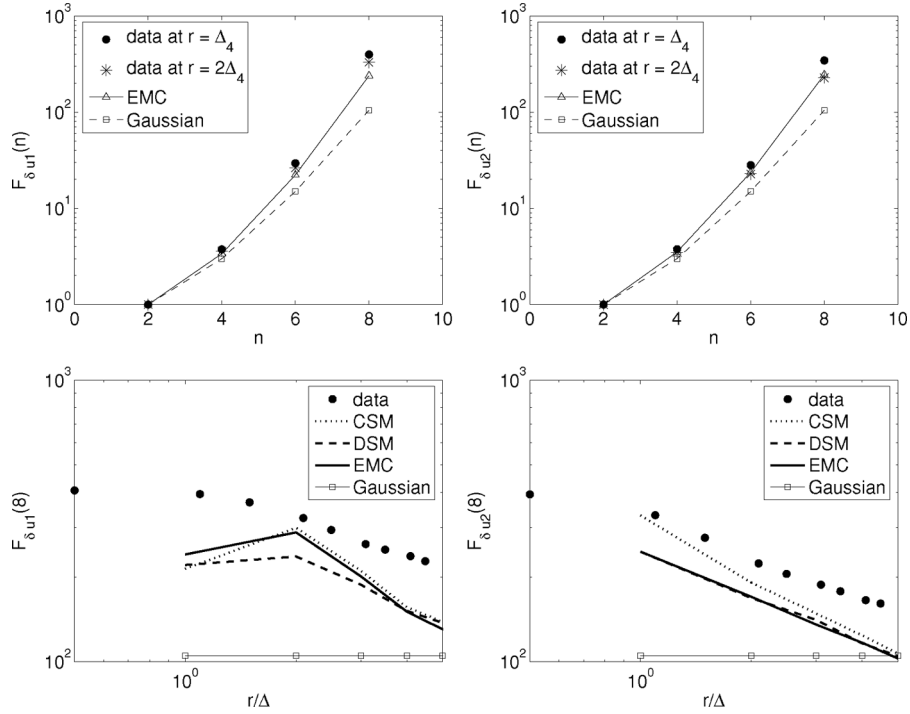


Figure 12. Comparison of the skewness coefficient with increasing correlation distance for the constant-coefficient Smagorinsky model (CSM) the dynamic Smagorinsky model (DSM) and ensemble mean closure (EMC).

The top two plots of figure 12 show results for the longitudinal ($i = 1$) and transverse ($i = 2$) hyper-flatness at various orders. Data are shown for two separation scales but the simulation results are presented only at $r = h$. The factors for a Gaussian variable are also presented for reference. Somewhat interestingly, the simulation matches very well with the transverse factors at $r = 2\Delta_4$ (recall $h = \Delta_4$). This is presumably another consequence of the implied filter kernel and seems more or less fortuitous. This trend continues, however, when examining the 8th order hyper-flatness factors (the two lower plots in figure 12) and the skewness coefficients in figure 13. The skewness coefficient is given by

$$S = \frac{\langle (\delta \tilde{U}_1)^3 \rangle}{\langle (\delta \tilde{U}_1)^2 \rangle^{3/2}}. \quad (75)$$

In these plots we also show comparisons for the constant coefficient Smagorinsky model [15] and the dynamic Smagorinsky model [2]. All three models exhibit similar behavior, matching the overall trends quite well, but the simulation results seem to be off by roughly one filter width. We attribute this discrepancy more to the numerical procedure (i.e. poor grid resolution for the given filter width) than to the residual stress model. Given that most engineering calculations are performed without explicit filtering it is prudent to examine and understand the limitation of model performance under these conditions. The skewness, in particular, seems to be strongly affected by the numerics at the scale $r = h$. At larger scales, however, the simulations recover the skewness trends quite well.

For reference we also present the PDFs of the production of residual kinetic energy and the τ_{12}^R component of the residual stress (computed for the north ucell face). These results are given in figures 14 and 15, respectively. The conclusions are similar to those found by Kang

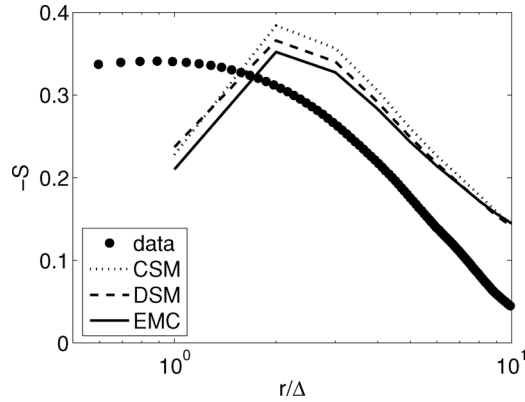


Figure 13. Comparison of the skewness coefficient with increasing correlation distance for the constant coefficient Smagorinsky model (CSM), the dynamic Smagorinsky model (DSM) and ensemble mean closure (EMC).

et al. [23] for the Smagorinsky and dynamic Smagorinsky models. As shown by figure 14, EMC is a purely dissipative model. The stress PDF shows results similar to the constant coefficient model and certainly does not capture the distribution shape as well as the mixed non-linear model of Anderson and Meneveau [23, 39] (results are presented in [39]). This is not surprising given that EMC only has the physics built in to model one part of a four part stress. Realistically, we should only expect EMC to capture first order effects such as energy dissipation. It would be interesting, however, to make similar comparisons with the low-Re data of the CBC experiment where the viscous effects are more prevalent.

5. Extension to passive scalar subgrid transport

The FV-LES transport equation for a passive scalar ‘cell average’, $\tilde{\phi}$, can be written as

$$\frac{d\tilde{\phi}}{dt} = -\frac{S_k}{V} n_{kj} \left(\overline{\phi}^{x_k} \tilde{U}_j^{(k)} + \Gamma \frac{\partial \overline{\phi}^{(k)}}{\partial x_j} + \tau_{\phi,j}^{R,(k)} \right), \quad (76)$$

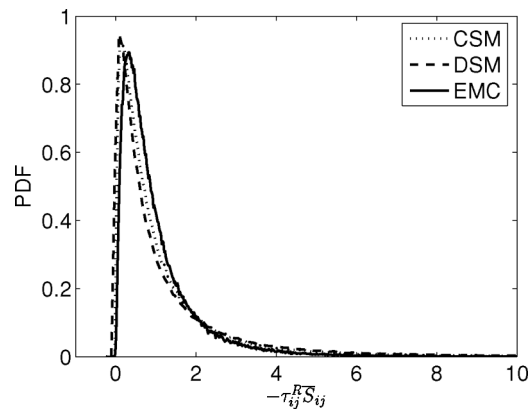


Figure 14. Production of residual kinetic energy for the constant coefficient Smagorinsky model (CSM), the dynamic Smagorinsky model (DSM) and ensemble mean closure (EMC).

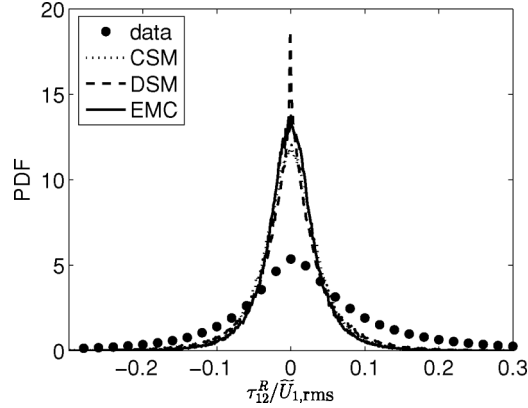


Figure 15. Residual shear stress PDF for the constant coefficient Smagorinsky model (CSM), the dynamic Smagorinsky model (DSM) and ensemble mean closure (EMC).

where the overbar is, again, a surface filter, Γ is the molecular scalar diffusivity, and

$$\tau_{\phi,j}^{R,(k)} \equiv \overline{\phi U_j^{(k)}} - \bar{\phi}^{x_k} \tilde{U}_j^{(k)} \quad (77)$$

is the unclosed residual scalar flux. Notice that the second term of the residual flux is again explicitly based on the numerical scheme. For Schmidt numbers $Sc \equiv \frac{\nu}{\Gamma} \geq 1$, the mixing rate of the scalar is strongly dependent on $\tau_{\phi,j}^R$ [12] and is a direct result of unresolved scalar advection.

The abstraction used for the turbulent flux in EMC is powerful in that it allows the method to be easily extended to model the subgrid terms for scalar transport without the need for turbulent Schmidt (Sc_t) or turbulent Prandtl (Pr_t) numbers (see, for example, [12, 13]). As a review of the EMC concept, the *scalar* is linearized (based on the local scalar gradient in the conceptual ODT line direction) and mapped (via the triplet map) at a rate determined by the time scale physics of the *velocity* field. Hence, the scalar mapping is tied to the ‘displacement’ function, e.g. (5), and the time scale, τ , is tied to the energy (or strain) of the velocity field. Because scalars are not subject to modification analogous to pressure-induced velocity scrambling during advection, kernel redistribution is not applied to scalars after a triplet mapping event [1]; this only simplifies matters for scalar EMC. In fact, in section 2.2 we have already worked out all the mathematics necessary to describe the scalar displacement. In direct analogy to the velocity linearization (see figure 1), the scalar is linearized as follows:

$$\varphi(r) = \mathcal{S}_\phi(y)r + b, \quad (78)$$

where $\mathcal{S}_\phi \equiv [\partial_r \bar{\phi}(r)]_{r=y}$ and, again, b drops out during the derivation. The scalar displacement function is, therefore, simply given by (6) with $\mathcal{S}_\phi(y)$ substituted for $\mathcal{S}(y)$. Leaving freedom to improve the time scale physics, we can then generalize the EMC approximation to (77), for $x_j = y$, as

$$\tau_{\phi,y}^R \approx R_\phi(y) = -\frac{2}{27} \mathcal{S}_\phi(y) \int_{l_{\min}}^{l_{\max}} \frac{l}{\tau} dl. \quad (79)$$

Here $R_\phi(y)$ denotes our model for the residual scalar flux. The time scale is based on the velocity (not scalar) field. Again, all the mathematics has been worked out in the previous

sections. Thus, for vanilla scalar EMC we have

$$R_\phi(y) = -\frac{1}{27}C_e(l_{\max}^2 - l_{\min}^2)|\mathcal{S}(y)|\mathcal{S}_\phi(y). \quad (80)$$

Note that $|\mathcal{S}(y)| = [\partial\bar{U}(r)]_{r=y}$. For an energy-based time scale we have

$$R_\phi(y) = -\frac{1}{27}\frac{C_e}{\sqrt{54}}(l_{\max}^2 - l_{\min}^2)|\mathcal{S}(y)|\mathcal{S}_\phi(y). \quad (81)$$

And for a Reynolds number-dependent time scale we have

$$R_\phi(y) = -\frac{1}{27}C_e\mathcal{F}(\text{Re}_h; Z, \nu)\mathcal{S}_\phi(y), \quad (82)$$

where \mathcal{F} is given by (38).

The models (80)–(82) do not make use of a turbulent Schmidt number. However, by comparing the scalar model with the momentum model we can deduce an implied turbulent Schmidt number for EMC and we find that Sc_t is dependent on the choice of α . Consider a canonical scalar flow problem in which a mean scalar gradient and a homogeneous shear are aligned. That is, $\mathcal{S}_\phi = \mathcal{S}_1$ and $\mathcal{S}_2 = \mathcal{S}_3 = 0$. To most clearly see the affect of α with regard to the implied turbulent Schmidt number, assume the flow is at high Re (i.e. $l_{\max} \gg l_{\min}$). We may then use equations (29) and (81) in our analysis. With the scalar and velocity strains equal we can determine the turbulent Schmidt number by (divide (29) by (81) for the specific conditions of the stated canonical problem)

$$\text{Sc}_t = \frac{1}{2} + \frac{1}{2}\sqrt{\beta_{11}}. \quad (83)$$

Therefore, recalling $\beta_{ij} = \delta_{ij} + \alpha T_{ij}$ (see section 2.3.2), for $\alpha = 0$ we have $\text{Sc}_t = 1$, for $\alpha = 2/3$ we have $\text{Sc}_t \approx 0.79$, and for $\alpha = 1$ we have $\text{Sc}_t = 1/2$. Hence, the value $\alpha = 2/3$, which is physically preferable based on equipartition of energy, puts the turbulent Schmidt number very near the accepted engineering *constant* value of 0.7 [12, 13]. In reality, the turbulent Schmidt and Prandtl numbers are not constant, however. They vary in space and time. Experimental evidence (see, for example, [40]) suggests that the values range from 0.7 to 0.9. EMC is a computationally cheap method for accounting for the local variation. Note that $\text{Sc}_t = 0.79$ (for $\alpha = 2/3$) is specific to the conditions of the canonical problem. The implied turbulent Schmidt number for EMC would vary spatially and temporally within a real flow simulation. It should be noted that the high Re version of the model was used here simply for clarity in the example. The Re -dependent version for scalar EMC (82) will also exhibit local variation in the turbulent Schmidt number and the model will turn off in regions of the flow where the velocity field is resolved.

6. Conclusions

Ensemble mean closure is an idealization of ODT and allows theoretical determination of the rate constant using Lilly's method [3]. The theoretical value, $C_e = 1.4\sqrt{54}$, worked well for the suite of validation tests presented here (with the caveat that the constant was derived based on $\alpha = 0$ and we subsequently found $\alpha = 2/3$ to yield slightly better results). This represents a significant improvement in our understanding of ODT (ultimately our model of interest). The factors $1/27$ and $1/\sqrt{54}$, for example, were previously buried in empirical tuning. Due to recursive mapping and the geometry of the triplet map, the rate constant for the full ODT model should be lower by roughly a factor of 3. Preliminary ODT results support this hypothesis

[8, 9]. Additionally, a computational method for direct evaluation of the ODT rate constant is identified that is analogous to the algebraic method applied to EMC.

EMC is a viable LES closure in its own right. The Reynolds number-dependent version includes a viscous cutoff parameter which represents the critical cell Reynolds number for an eddy turnover and addresses the problem of finite eddy viscosity without using the dynamic procedure. The low Re wind tunnel data of Comte-Bellot and Corrsin [37] was used to empirically determine the cutoff value ($Z \approx 3.0$). Good results are obtained for decaying isotropic turbulence simulations at two Taylor scale Reynolds numbers differing by an order of magnitude. No explicit filtering step was required in these cases, making the overall approach attractive for engineering calculations. It has been shown that the EMC concept can be extended in a straightforward way to model the residual advective transport of scalars in LES, providing a consistent link between subgrid momentum and scalar transport without the need for *a priori* specification of turbulent Schmidt and Prandtl numbers. Moreover, EMC yields a theoretical prediction of these quantities that agrees with empirical estimates.

The utility of EMC extends beyond LES closure. Many problems in engineering, meteorology and astrophysics reach Reynolds numbers where even resolving ODT down to the dissipative scales is too expensive. EMC is the prime candidate for subgrid closure of ODT in this case. Schmidt *et al.* [8] used EMC as the subgrid closure for ODT, which in turn was the subgrid closure for an LES of decaying isotropic turbulence, showing proof of concept of what is truly a multiscale modeling approach. The efficacy of this strategy has been demonstrated by a geophysical flow application [21].

Further work is required to determine the implications of the present theoretical framework with regard to the full ODT model. In full ODT an optimal value for l_{\max} will exist. Variation of l_{\max} is directly offset by variation in C_e , through Lilly's analysis (i.e. l_{\max} and C_e are not independent parameters) and so in EMC the specific value of the length scale is unimportant; how one computes the local strain is really what determines the filter width. In full ODT, however, stochastic backscatter and subgrid statistics can be modeled and the specific C_e - l_{\max} combination can affect the results significantly.

Acknowledgements

Funding for this work was provided through a Department of Energy Computational Science Graduate Fellowship (DE-FG02-97ER25308). This work was partially supported by the US Department of Energy, Office of Basic Energy Sciences, Division of Chemical Sciences, Geosciences, and Biosciences. Sandia National Laboratories is a multi-program laboratory operated by Sandia Corporation, a Lockheed Martin Company, for the US Department of Energy under contract DE-AC04-94-AL85000. We would like to especially thank Tom Smith for his isotropic turbulence initialization code, Steve de Bruyn Kops for insightful discussions regarding initialization and Chris Kennedy for help with his high order interpolants.

Appendix A. Finite volume flux symmetry

Here we clarify what is meant by 'symmetry' of the finite volume surface fluxes, show that they are symmetric to second order in space and give a simple flow example to show that these fluxes are not identically symmetric in general.

The residual stress on a surface of a control volume (CV) is defined as

$$\tau_{ij}^R \equiv \overline{U_i U_j} - \overline{U_i} \overline{U_j}. \quad (84)$$

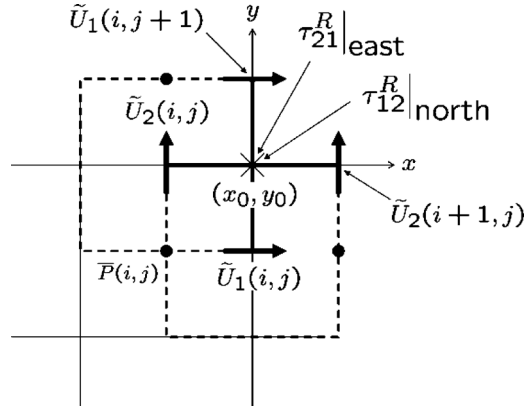


Figure A1. Staggered grid ucell and vcell surface fluxes. The origin of the Taylor expansion (x_0, y_0) is marked by the \times .

Here we will consider a simple two-dimensional example, so let the overbar represent a tophat filter in one dimension along a CV surface (consider the ‘north’ face at (x, y) , for example):

$$\bar{\phi}(x, y) \equiv \int_{x-h/2}^{x+h/2} \phi(x', y) dx'. \quad (85)$$

The stress defined by (84) is obviously symmetric on a surface. This is not of concern in the FV formulation, however, because the stress is dotted with the surface normal unit vector to obtain the flux. The flux symmetry comes into question for staggered schemes (see figure A1) where on a uniform grid, for example, ‘symmetry’ would imply that τ_{12}^R on the north face of a U momentum CV (ucell) is equal to τ_{21}^R on the east face of a vcell. Indeed, the staggered arrangement makes this symmetry easy to achieve since the strain rate is computed as

$$\begin{aligned} \bar{S}_{12}|_{\text{north ucell}} &= \bar{S}_{21}|_{\text{east vcell}} \\ &= \frac{1}{2} \left(\frac{\tilde{U}_1(i, j+1) - \tilde{U}_1(i, j)}{h} + \frac{\tilde{U}_2(i+1, j) - \tilde{U}_2(i, j)}{h} \right), \end{aligned} \quad (86)$$

for both the north ucell and east vcell faces (taking the discrete divergence yields a symmetric positive definite diffusive operator [26]). For second-order staggered schemes (e.g. Harlow and Welch [33]) the second term in [84] is computed as

$$\bar{U}_1 \bar{U}_2|_{\text{north}} = \bar{U}_2 \bar{U}_1|_{\text{east}} = \left(\frac{\tilde{U}_1(i, j) + \tilde{U}_1(i, j+1)}{2} \right) \left(\frac{\tilde{U}_2(i, j) + \tilde{U}_2(i+1, j)}{2} \right) \quad (87)$$

and is symmetric. Therefore, any asymmetry in $\overline{U_i U_j}$ should be captured by the residual stress model. Consider, for example, the Taylor expansion of the north ucell stress. As in the sketch in figure A1, let the origin lie at the intersection of the north ucell face and the east vcell face (call this point (x_0, y_0)):

$$\begin{aligned} \overline{U_1 U_2}|_{\text{north}}(x_0, y_0) &= \frac{1}{h} \int_{-h/2}^{h/2} U_1 U_2(x - x_0, y_0) dx \\ &= \frac{1}{h} \int_{-h/2}^{h/2} \left(U_1 U_2|_{(x_0, y_0)} + (x - x_0) \frac{\partial U_1 U_2}{\partial x} \Big|_{(x_0, y_0)} \right) dx \end{aligned}$$

$$\begin{aligned}
& + \frac{(x - x_0)^2}{2} \frac{\partial^2 U_1 U_2}{\partial x^2} \Big|_{(x_0, y_0)} + \dots \Big) dx \\
& = U_1 U_2 \Big|_{(x_0, y_0)} + \frac{h^2}{24} \frac{\partial^2 U_1 U_2}{\partial x^2} \Big|_{(x_0, y_0)} + \dots
\end{aligned} \tag{88}$$

Similarly, the east vcell advective flux is

$$\overline{U_2 U_1} \Big|_{\text{east}(x_0, y_0)} = U_2 U_1 \Big|_{(x_0, y_0)} + \frac{h^2}{24} \frac{\partial^2 U_2 U_1}{\partial y^2} \Big|_{(x_0, y_0)} + \dots \tag{89}$$

Subtracting (89) from (88) yields the asymmetry in the surface fluxes, which is second order for the uniform grid case (all terms evaluated at (x_0, y_0)):

$$\overline{U_1 U_2} \Big|_{\text{north}} - \overline{U_2 U_1} \Big|_{\text{east}} = \frac{h^2}{24} \left[\frac{\partial^2 U_1 U_2}{\partial x^2} - \frac{\partial^2 U_2 U_1}{\partial y^2} \right] + \dots \tag{90}$$

As a simple example illustrating that (90) is not zero in general consider the flow field

$$\begin{aligned}
U_1(x, y) &= ax + by, \\
U_2(x, y) &= cx - ay,
\end{aligned} \tag{91}$$

where a , b and c are constants. This field obeys continuity $\partial_x U_1 + \partial_y U_2 = a - a = 0$, but upon substitution into (90) yields

$$\overline{U_1 U_2} \Big|_{\text{north}} - \overline{U_2 U_1} \Big|_{\text{east}} = \frac{h^2}{12} [a(b + c)] + \dots \tag{92}$$

If $b = c$ the flow is irrotational ($\omega_z = \partial_y U_1 - \partial_x U_2 = b - c$) but the fluxes are still not identically symmetric.

Appendix B. Derivation of Reynolds number-dependent closure

Here we go through the derivation of (33). Using the kernel-based momentum displacement (section 2.3.1) we can write

$$\begin{aligned}
R_i(y) &= \int_{l_{\min}}^{l_{\max}} \frac{1}{\tau} \int_{y-l}^y \frac{\psi_i(y; y_0, l)}{l^2} dy_0 dl, \\
&= \underbrace{-\frac{2}{27} \left(\frac{1}{2} \mathcal{S}_i(y) + \frac{1}{2} \text{sgn}(\mathcal{S}_i(y)) \sqrt{\beta_{ij} \mathcal{S}_j^2(y)} \right)}_A \int_{l_{\min}}^{l_{\max}} \frac{l}{\tau} dl, \\
&= AC_e \int_{l_{\min}}^{l_{\max}} l \left(\frac{1}{54} \sum_j \mathcal{S}_j^2(y) - \frac{Z^2 v^2}{l^4} \right)^{1/2} dl.
\end{aligned} \tag{93}$$

At this point we make the following change of variables. Let

$$R_i(y) = AC_e \int_{l_{\min}}^{l_{\max}} l \sqrt{a^2 - x^2} dl, \tag{94}$$

where

$$a^2 = \frac{1}{54} \sum_j \mathcal{S}_j^2(y) \quad \text{and} \quad x^2 = \frac{Z^2 v^2}{l^4}. \tag{95}$$

Hence,

$$l = (Zv)^{\frac{1}{2}}x^{-\frac{1}{2}} \quad \text{and} \quad dl = -\frac{1}{2}(Zv)^{\frac{1}{2}}x^{-\frac{3}{2}} dx. \quad (96)$$

Substituting these changes into (94) yields

$$\begin{aligned} R_i(y) &= AC_e \int_{x_{\min}}^{x_{\max}} \overbrace{[(Zv)^{\frac{1}{2}}x^{-\frac{1}{2}}]}^l \sqrt{a^2 - x^2} \overbrace{\left[-\frac{1}{2}(Zv)^{\frac{1}{2}}x^{-\frac{3}{2}} dx\right]}^{dl}, \\ &= AC_e \left(-\frac{1}{2}\right) Zv \int_{x_{\min}}^{x_{\max}} \frac{\sqrt{a^2 - x^2}}{x^2} dx. \end{aligned} \quad (97)$$

The limits of integration are $x_{\min} = Zv/l_{\min}^2$ and $x_{\max} = Zv/l_{\max}^2$.

From integral tables we find that

$$\int \frac{\sqrt{a^2 - x^2}}{x^2} dx = -\sin^{-1}\left(\frac{x}{a}\right) - \frac{\sqrt{a^2 - x^2}}{x} + C. \quad (98)$$

Hence,

$$\begin{aligned} R_i(y) &= AC_e \left(-\frac{1}{2}\right) Zv \left[-\sin^{-1}\left(\frac{x}{a}\right) - \frac{\sqrt{a^2 - x^2}}{x} \right]_{Zv/l_{\min}^2}^{Zv/l_{\max}^2}, \\ &= AC_e \left(-\frac{1}{2}\right) Zv \left[\sin^{-1}\left(\frac{Zv}{al_{\min}^2}\right) + \frac{\sqrt{a^2 - \left(\frac{Zv}{l_{\min}^2}\right)^2}}{\frac{Zv}{l_{\min}^2}} \right. \\ &\quad \left. - \sin^{-1}\left(\frac{Zv}{al_{\max}^2}\right) - \frac{\sqrt{a^2 - \left(\frac{Zv}{l_{\max}^2}\right)^2}}{\frac{Zv}{l_{\max}^2}} \right], \\ &= -\frac{1}{2} AC_e \left[\sqrt{a^2 l_{\min}^4 - (Zv)^2} - \sqrt{a^2 l_{\max}^4 - (Zv)^2} \right. \\ &\quad \left. + Zv \left(\sin^{-1}\left(\frac{Zv}{al_{\min}^2}\right) - \sin^{-1}\left(\frac{Zv}{al_{\max}^2}\right) \right) \right], \end{aligned} \quad (99)$$

recovering (33) and (34).

Appendix C. Numerical implementation details for EMC

Here we detail the numerical implementation for EMC with a staggered grid arrangement. Perhaps the most clear and concise way to describe this implementation is to follow a two-dimensional example. The same ideas are easily extended to three dimensions. This particular implementation was chosen to maintain consistency with full ODT closure for LES [8, 9] where the ODT lattice lines intersect at the pressure cell (pcell) center.

To avoid confusion related to component indexing and grid indexing we will use $[U, V]$ instead of $[U_1, U_2]$ to represent the velocity components. Here keep in mind that the index pair

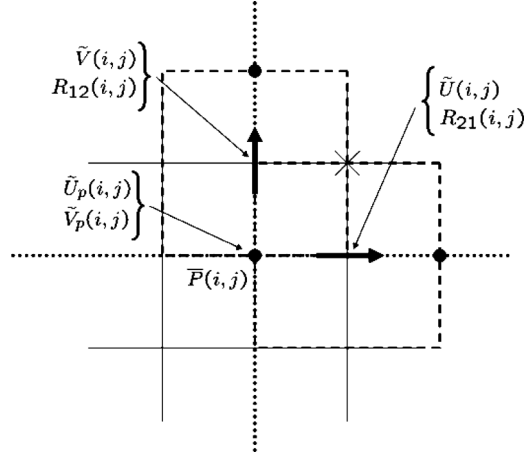


Figure C1. Staggered grid arrangement for computing EMC stresses. The small dotted (not dashed) lines crossing at the pcell center represent an ODT lattice.

(i, j) represents a computational storage location, *not* a discrete spatial location. Figure C1 shows the staggered grid layout. The solid dots represent the pcell center. The right arrow represents the storage location and center of a u momentum cell (ucell) and the up arrow is a v momentum cell center (vcell).

The first step in computing the stress is to interpolate the ucell and vcell velocities to the pcell location. These are stored as \tilde{U}_p and \tilde{V}_p . We use the 10th-order interpolation of Kennedy [41]. We use (33) as the EMC model with (38) employed for \mathcal{F} . Evaluating the stress for a given direction reduces to evaluating the velocity gradient vector for that direction.

C.1 Diagonal components

The diagonal components of the stress are computed and stored at the pcell center. Here we will need the full velocity gradient tensor.

$$\begin{aligned}
 \partial_x \bar{U} |_{\text{pcell}} &\approx \frac{\tilde{U}(i, j) - \tilde{U}(i-1, j)}{h}, \\
 \partial_x \bar{V} |_{\text{pcell}} &\approx \frac{\tilde{V}_p(i+1, j) - \tilde{V}_p(i-1, j)}{2h}, \\
 \partial_y \bar{U} |_{\text{pcell}} &\approx \frac{\tilde{U}_p(i, j+1) - \tilde{U}_p(i, j-1)}{2h}, \\
 \partial_y \bar{V} |_{\text{pcell}} &\approx \frac{\tilde{V}(i, j) - \tilde{V}(i, j-1)}{h}.
 \end{aligned} \tag{100}$$

C.2 Off-diagonal components

We store R_{21} at the ucell location for easy averaging over the vcell east and west faces:

$$\partial_x \bar{U} |_{\text{ucell}} \approx \frac{\tilde{U}_p(i+1, j) - \tilde{U}_p(i, j)}{h},$$

$$\partial_x \bar{V} |_{\text{ucell}} \approx \frac{\tilde{V}_p(i+1, j) - \tilde{V}_p(i, j)}{h}. \quad (101)$$

We store R_{12} at the vcell location for easy averaging over the ucell north and south faces:

$$\begin{aligned} \partial_y \bar{U} |_{\text{vcell}} &\approx \frac{\tilde{U}_p(i, j+1) - \tilde{U}_p(i, j)}{h}, \\ \partial_y \bar{V} |_{\text{vcell}} &\approx \frac{\tilde{V}_p(i, j+1) - \tilde{V}_p(i, j)}{h}. \end{aligned} \quad (102)$$

C.3 Computing the stress divergence

The average of the diagonal components is subtracted and the deviatoric part used in the computation (here q, r, s are component indices),

$$R_{qr}^d = R_{qr} - \delta_{qr} R_{ss}. \quad (103)$$

For the ucell the R_{11} stress is located on the east and west faces of a ucell CV. The north and south face stresses require averaging. Referring to (65), the discrete approximation to the subgrid force is given by (k is a component index and summation is implied)

$$\frac{\delta R_{1k}}{\delta x_k}(i, j) = \frac{R_{11}^d(i+1, j) - R_{11}^d(i, j)}{h} + \frac{\overline{R_{12}^d}(i, j) - \overline{R_{12}^d}(i, j-1)}{h}, \quad (104)$$

where

$$\overline{R_{12}^d}(i, j) = \frac{R_{12}^d(i, j) + R_{12}^d(i+1, j)}{2}. \quad (105)$$

Similarly, for the vcell we have

$$\frac{\delta R_{2k}}{\delta x_k}(i, j) = \frac{R_{22}^d(i, j+1) - R_{22}^d(i, j)}{h} + \frac{\overline{R_{21}^d}(i, j) - \overline{R_{21}^d}(i-1, j)}{h}, \quad (106)$$

where

$$\overline{R_{21}^d}(i, j) = \frac{R_{21}^d(i, j) + R_{21}^d(i, j+1)}{2}. \quad (107)$$

References

- [1] Kerstein, A.R., Ashurst, W.T., Wunsch, S. and Nilsen, V., 2001, One-dimensional turbulence: vector formulation and application to free shear flows. *Journal of Fluid Mechanics*, **447**, 85–109.
- [2] Germano, M., Piomelli, U., Moin, P. and Cabot, W., 1991, A dynamic subgrid-scale eddy viscosity model. *Physics of Fluids A*, **3**, 1760–1765.
- [3] Lilly, D.K., 1967, The representation of small-scale turbulence in numerical simulation experiments. In *Proceedings of the IBM Scientific Computing Symposium on Environmental Sciences* (Yorktown Heights, New York: IBM).
- [4] Pierre Sagaut., 2001, *Large Eddy Simulation for Incompressible Flows* (Berlin: Springer).
- [5] Kerstein, A.R., 1999, One-dimensional turbulence: model formulation and application to homogeneous turbulence, shear flows, and buoyant stratified flows. *Journal of Fluid Mechanics*, **392**, 277–334.
- [6] Pope, S.B., 2004, Ten questions concerning the large-eddy simulation of turbulent flows. *New Journal of Physics*, **6**.
- [7] Schmidt, R.C., Kerstein, A.R., Wunsch, S. and Nilsen, V., 2003, Near-wall LES closure based on one-dimensional turbulence modeling. *Journal of Computational Physics*, **186**, 317–355.
- [8] Schmidt, R.C., McDermott, R. and Kerstein, A., 2005, ODTLES: A Model for 3D Turbulent Flow Based on One-dimensional Turbulence Modeling Concepts, Report 2005–0206 (Albuquerque, New Mexico: Sandia National Laboratories).
- [9] McDermott, R.J., 2005, Toward one-dimensional turbulence subgrid closure for large-eddy simulation. PhD thesis, University of Utah.

- [10] Kerstein, A.R., 1988, A linear-eddy model of turbulent scalar transport and mixing. *Combustion Science and Technology*, **60**, 391–421.
- [11] Kerstein, A.R., 1991, Linear-eddy modelling of turbulent transport. Part 6. Microstructure of diffusive scalar mixing fields. *Journal of Fluid Mechanics*, **231**, 361–394.
- [12] Fox, R.O., 2003, *Computational Models for Turbulent Reacting Flows* (Cambridge: Cambridge University Press).
- [13] Norbert Peters, 2000, *Turbulent Combustion* (Cambridge: Cambridge University Press).
- [14] Sankaran, V., Porumbel, I. and Menon, S., 2003, Large-eddy simulation of single-cup gas-turbine combustor flows. In *39th AIAA Joint Propulsion Conference: AIAA 2003-5083*.
- [15] Smagorinsky, J., 1963, General circulation experiments with the primitive equations. *Monthly Weather Review*, **91**, 99–106.
- [16] Moin, P., Squires, K., Cabot, W. and Lee, S., 1991, A dynamic subgrid-scale model for compressible turbulence and scalar transport. *Physics of Fluids A*, **3**, 2746–2757.
- [17] Kerstein, A.R., 2003, Nonlocal first-order closure based on ODT. Unpublished.
- [18] Pope, S.B., 2000, *Turbulent Flows* (Cambridge: Cambridge University Press).
- [19] Ashurst, W.T. and Kerstein, A.R., 2005, One-dimensional turbulence: variable-density formulation and application to mixing layers. *Physics of Fluids*, **17**, 025107-1–025107-26.
- [20] Wunsch, S. and Kerstein, A., 2001, A model for layer formation in stably stratified turbulence. *Physics of Fluids*, **13**, 703–712.
- [21] Kerstein, A.R. and Wunsch, S., In press, Simulation of a stably stratified atmospheric boundary layer using one-dimensional turbulence. *Boundary Layer Meteorology*.
- [22] Meneveau, C. and Lund, T.S., 1997, The dynamic Smagorinsky model and scale-dependent coefficients in the viscous range of turbulence. *Physics of Fluids*, **9**, 3932–3934.
- [23] Kang, H.S., Chester, S. and Meneveau, C., 2003, Decaying turbulence in an active-grid-generated flow and comparisons with large-eddy simulation. *Journal of Fluid Mechanics*, **480**, 129–160.
- [24] Schumann, U., 1975, Subgrid scale model for finite difference simulation of turbulent flows in plane channels and annuli. *Journal of Computational Physics*, **18**, 376–404.
- [25] Lomax, H., Pulliam, T.H. and Zingg, D.W., 2001, *Fundamentals of Computational Fluid Dynamics* (Berlin: Springer).
- [26] R.W. Versteappen, C.P. and A. Veldman, E.P., 2003, Symmetry-preserving discretization of turbulent flow. *Journal of Computational Physics*, **187**, 343–368.
- [27] Ham, F.E., Lien, F.S. and Strong, A.B., 2002, A fully conservative second-order finite difference scheme for incompressible flow on non-uniform grids. *Journal of Computational Physics*, **177**, 117–133.
- [28] Morinishi, Y., Lund, T.S., Vasilyev, O.V. and Moin, P., 1998, Fully conservative high order finite difference schemes for incompressible flow. *Journal of Computational Physics*, **143**, 90–124.
- [29] Harten, A., 1989, ENO schemes with subcell resolution. *Journal of Computational Physics*, **83**, 148–184.
- [30] Shu, C.W., 1997, Essentially non-oscillatory and weighted essentially non-oscillatory schemes for hyperbolic conservation laws. NASA/CR-97-206253 ICASE Report No. 97-65. Available online at: <http://www.icase.edu/library/reports/rdp/97/97-65RDP.refer.html>
- [31] Leonard, A., 1974, Energy cascade in large eddy simulation of turbulent fluid flow. *Advances in Geophysics*, **18A**, 237–248.
- [32] Bardina, J., Ferziger, J.H. and Reynolds, W.C., 1980, Improved subgrid-scale models for large-eddy simulation. AIAA, 980–1357. American Institute of Aeronautics and Astronautics, Fluid and Plasma Dynamics Conference, 13th, Snowmass, Colo., July 14–16, 1980.
- [33] Harlow, F.H. and Welch, J.E., 1965, Numerical calculation of time-dependent viscous incompressible flow of fluid with a free surface. *Physics of Fluids*, **8**, 2182–2189.
- [34] Shu, C.W. and Osher, S., 1988, Efficient implementation of essentially non-oscillatory shock-capturing schemes. *Journal of Computational Physics*, **77**, 439–471.
- [35] Suresh, A. and Huynh, H.T., 1997, Accurate monotonicity-preserving schemes with Runge-Kutta time stepping. *Journal of Computational Physics*, **136**, 83–99.
- [36] Chorin, A.J. and Marsden, J.E., 1990, *A Mathematical Introduction to Fluid Mechanics*, 3rd Edn (New York: Springer).
- [37] Comte-Bellot, G. and Corrsin, S., 1971, Simple Eulerian time correlation of full- and narrow-band velocity signals in grid-generated, ‘isotropic’ turbulence. *Journal of Fluid Mechanics*, **48**, 273–337.
- [38] de Bruyn Kops, S.M., 1999, Numerical simulation of non-premixed turbulent combustion. PhD thesis, University of Washington.
- [39] Anderson, R. and Meneveau, C., 1999, Effects of the similarity model in finite-difference LES of isotropic turbulence using a Lagrangian dynamic mixed model. *Flow Turbulence and Combustion*, **62**, 201–225.
- [40] Chang, K. and Cowen, A., 2002, Turbulent Prandtl number in neutrally buoyant turbulent round jet. *Journal of Engineering Mechanics*, **128**, 1082–1087.
- [41] Kennedy, C.A. and Carpenter, M.H., 1994, Several new numerical methods for compressible shear-layer simulations. *Applied Numerical Mathematics*, **14**, 397–433.
- [42] Misra, A. and Pullin, D., 1997, A vortex-based subgrid stress model for large-eddy simulation. *Physics of Fluids*, **9**, 2443–2454.